IEA COMPARISON OF LONGWAVE RADIOMETERS

A Technical Report of Task 9:

Solar Radiation and Pyranometry Studies

July 1993

INTERNATIONAL ENERGY AGENCY
Solar Heating & Cooling Programme

THE INTERNATIONAL ENERGY AGENCY
SOLAR HEATING AND COOLING PROGRAMME

International Energy Agency

The International Energy Agency, headquartered in Paris, was formed in November 1974 as an autonomous body within the framework of the Organization for Economic Cooperation and Development to establish cooperation in the area of energy policy. Twenty-one countries are presently members, with the Commission of the European Communities participating under a special arrangement.

Collaboration in the research, development and demonstration of new energy technologies to help reduce dependence on oil and to increase long-term energy security has been an important part of the Agency's programme. The IEA R&D activities are headed by the Committee on Research and Development (CRD) which is supported by a small Secretariat staff. In addition, four Working Parties (in Conservation, Fossil Fuels, Renewable Energy and Fusion) are charged with monitoring the various collaborative energy Agreements, identifying new areas for cooperation and advising the CRD on policy matters.

Solar Heating and Cooling Programme

On of the first collaborative R&D agreements was the IEA Solar Heating and Cooling Programme which was initiated in 1977 to conduct joint projects in active and passive solar technologies, primarily for building applications. The twenty members of the Programme are:

Australia	France	Spain
Austria	Germany	Sweden
Belgium	Italy	Switzerland
Canada	Japan	Turkey
Denmark	Netherlands	United Kingdom
European Community	New Zealand	United States
Finland	Norway	

A total of nineteen projects or "Tasks" have been undertaken since the beginning of the Programme. The overall programme is managed by an Executive Committee composed of one representative from each of the member countries, while the leadership and management of the individual Tasks is the responsibility of Operating Agents. These Tasks and their respective Operating Agents are:

*Task 1:	Investigation of the Performance of Solar Heating and Cooling Systems - Denmark
*Task 2:	Coordination of Research and Development on Solar Heating and Cooling - Japan
*Task 3:	Performance Testing of Solar Collectors - United Kingdom
*Task 4:	Development of an Insolation Handbook and Instrument Package - United States
*Task 5:	Use of Existing Meteorological Information for Solar Energy Application - Sweden
*Task 6:	Solar Heating, Cooling, and Hot Water Systems Using Evacuated Collectors - United States
*Task 7:	Central Solar Heating Plants with Seasonal Storage - Sweden
*Task 8:	Passive and Hybrid Solar Low Energy Buildings - United States
*Task 9:	Solar Radiation and Pyranometry Studies - Germany
*Task 10:	Material Research and Testing - Japan
*Task 11:	Passive and Hybrid Solar Commercial Buildings - Switzerland
Task 12:	Building Energy Analysis and Design Tools for Solar Applications - United States
Task 13:	Advanced Solar Low Energy Buildings - Norway
Task 14:	Advanced Active Solar Systems - Canada
Task 16:	Photovoltaics in Buildings - Germany
Task 17:	Measuring and Modelling Spectral Radiation - Germany
Task 18:	Advanced Glazing Materials - United Kingdom
Task 19:	Solar Air Heating - Switzerland (in planning stage)
Task 20:	Solar Retrofit Systems for Buildings - Sweden (in planning stage)

*Completed Task

Report No. IEA-SHCP-9F-3

IEA COMPARISON OF LONGWAVE RADIOMETERS

Klaus Dehne

Uwe Bergholter

Fritz Kasten

Deutscher Wetterdienst
Meteorologisches Observatorium Hamburg

Frahmredder 95
D-22393 Hamburg
Germany

July 1993

This report documents work performed within the IEA Solar Heating and Cooling Programme
Task 9: Solar Radiation and Pyranometry
Subtask F: Irradiance Measurement for Solar Collector Testing

Additional copies may be ordered at a price of 10.-- DM plus postage from:

Deutscher Wetterdienst
Meteorologisches Observatorium Hamburg
Postfach 65 01 50
D-22361 Hamburg
Germany

Distribution Category: Unrestricted

CONTENTS

EXECUTIVE SUMMARY

As activity in the field of solar energy research and application increased, a need was identified for more accurate solar radiation and meteorological data to aid in resource assessment, simulation model development and validation, system design and evaluation, collector testing, and others. Not least through the activities of Task 9 Subtasks C and F, the techniques of measuring solar radiation have appreciably been improved during the past years so that the measuring uncertainty of the best systems has now reached the 1 percent level.

On the other hand, the present day accuracy of measuring terrestrial radiation, also called infrared or thermal or longwave radiation, is far from being satisfactory. Longwave radiation plays an important role in the energy balance of solar systems and buildings. The longwave radiation of the sky hemisphere, also called (downwelling) atmospheric radiation, is presently measured with an uncertainty of about ± 10 %.

The aim of the comparison of hemispherical longwave radiation measurement procedures under Task 9, Subtask F was:

- to assess the state of the art of measuring techniques, systems, and instruments which are operationally used in various countries,
- to analyze the calibration techniques used and the deviations of calibration factors derived by various laboratories,
- to recommend measures and procedures for improving measuring and calibration techniques.

The comparison was performed at Meteorologisches Observatorium Hamburg of Deutscher Wetterdienst from July 1989 to April 1990. Six IEA member countries participated with eight measuring systems. In the analyses, first the diurnal and seasonal variations of atmospheric radiation A as measured by the different systems were established. Second, comparisons of radiometer temperatures were performed in order to possibly explain differences of the measured A-values. Third, the dependence of measured A-values on the accuracy of the responsivities and correction factors of the radiometers was investigated. Finally, computer methods of adjusting the measured A-values were tested.

The comparison has demonstrated that the measuring uncertainty of hourly means of atmospheric radiation with simultaneous high global solar radiation is about ± 10 % but considerably less at clouded sky and at night.

The main sources of the observed differences between the measured A-values are the relatively large differences of calibration and correction factors determined by different laboratories. This result calls for substantial effort on improving and standardizing the calibration technique for longwave radiometers. None the less, there are several practical measures which have already been proven useful to avoid or reduce measuring errors during the comparison; they are therefore recommended generally. The two most important are

- Ventilation of the radiometer dome in order to avoid deposition of dew and rime and to level the dome temperature at the air temperature.

- Shading of the pyrgeometer dome by a sun-following shade-disk in order to prevent heating by direct solar radiation.

These recommendations have already been taken as rules for the measurement of atmospheric radiation within the worldwide Baseline Surface Radiation Network (BSRN).

Participation:

Institutions from six IEA member countries participated in the comparison:

AES: Atmospheric Environment Service, 4905 Dufferin Street, Downsview, Ontario M3H 5T4, Canada (D. Wardle)

EKO: EKO Instruments Trading Co., Ltd., 21-8, Hatagaya 1 chome, Shibuya-ku, 151 Tokyo, Japan (Y. Miyake)

MOH: Deutscher Wetterdienst, Meteorologisches Observatorium Hamburg, Frahmredder 95, D-22393 Hamburg, Germany (K. Dehne)

MRF: Meteorological Office, Meteorological Research Flight, Instrument Section, Farnborough, Hants. GU14 6TD, U.K. (J. Seymour)

NASA: NASA Langley Research Center, Radiation Sciences Branch, MS 420, Hampton, VA 23665-5221, U.S.A. (C. Whitlock)

SMHI: Swedish Meteorological and Hydrological Institute, S-60176 Norrköping, Sweden (L. Dahlgren)

1. INTRODUCTION

As activity in the field of solar energy research and application increased, a need was identified for more accurate solar radiation and meteorological data to aid in resource assessment, system design and evaluation, and solar collector testing. Task 9 was initiated to address this need and to expand on the work accomplished in earlier IEA meteorological Tasks (4 and 5). The first phase of the Task ran from October 1982 until June 1987 and consisted of three Subtasks, each coordinated by a lead country:

- Subtask A: Small-Scale Time and Space Variability of Solar Radiation (Austria)
- Subtask B: Validation of Solar Irradiance Simulation Models (Canada)
- Subtask C: Pyranometry (Canada)

The second phase of the Task ran from July 1987 until June 1991. The work was divided into the following Subtasks:

- Subtask D: Techniques for Supplementing Network Data for Solar Energy Applications (Switzerland)
- Subtask E: Representative Design Years for Solar Energy Applications (Denmark)
- Subtask F: Irradiance Measurement for Solar Collector Testing (Canada)

Based on some of the results obtained in Subtasks A and B, Subtask D was evaluating techniques for estimating solar energy radiation resources at locations between network sites, using both measured and synthetic data. In addition to the classical statistical techniques for deriving solar radiation data received at the earth's surface (e.g., interpolation and extrapolation), new methods, such as satellite-based techniques, were investigated.

As an alternative to measured meteorological data, several techniques have been developed recently for simulating representative hourly data over the year using statistical techniques. This approach is particularly suited to simplified design techniques since there are no uncontrolled variables. Subtask E was concerned with developing recommendations on the most appropriate methods for producing representative design years as input to solar energy system and building energy system simulation models.

Building on the work of Subtask C, Subtask F focused on demonstrating the improved quality of solar radiation measurements now available. Participants developed guidelines on solar radiation measurement for solar energy engineers and predicted achievable accuracies for such measurements. Further experimental work on characterization of pyranometers was conducted, and the improvement of terrestrial (longwave) radiation measurement for solar collector testing was investigated.

The measurement of downwelling thermal radiation of the atmosphere during outdoor tests or of solar simulator thermal radiation during indoor tests of solar collectors is highly recommended because longwave radiation significantly affects the performance of the collectors. Two methods developed and applied in meteorology are available for the measurement of the hemispherical longwave irradiance (wavelengths $> 3\ \mu m$):

- the determination of the difference between the hemispherical total irradiance (0.3 μm to $> 50\ \mu m$) measured by a **pyrradiometer** and the hemispherical solar irradiance (0.3 μm to 3 μm) measured by a **pyranometer**;

- the direct measurement by a **pyrgeometer**.

The disadvantages of the first (and older) method are the use of two radiometers and some practical problems with the polyethylene dome generally used in pyrradiometry. The main problem of the pyrgeometer is the non-ideal transmittance of the silicon dome which is covered by a cut-off interference filter to define the lower limit of the spectral transmittance at about 4 μm.

The differences in determining the hemispherical longwave radiation by different meteorological institutes are not only caused by the different radiometer types used but also by different ventilation systems and by different correction procedures. The measurement uncertainty of the hemispherical longwave radiation is in the order of ± 10 %. No reference instrument is available up to now. The absolute longwave calibration is established by blackbody radiators.

The aim of the comparison of hemispherical longwave radiation measurement procedures under IEA SHCP Task 9, Subtask F was

- to find out the state-of-the-art of procedures internationally used, expecially the level of measurement uncertainty and its dependence on meteorological conditions,

- to find out the extent of deviation of calibration factors derived by different institutes,

- to recommend improved procedures for reducing the measurement uncertainty with the goal to establish a reference,

- to recommend measurement procedures which are particularly suited for solar collector testing.

2. MEASUREMENTS

2.1 Participating radiometers

Six IEA member countries participated in the comparison with 6 pyrgeometers and 2 pyrradiometers. The instruments are listed on Table 1. The columns contain type, serial number, owner's institution, type of temperature sensor and ventilation device used as well as the evaluation formula recommended by the owner.

Four of the pyrgeometers are Eppley radiometers of the type PIR; an additional pyrgeometer had been equipped by J.S. Foot (Meteorological Research Flight, Farnborough) with a special thermopile to reduce the influence of the internal temperature gradients on the measuring signal. The PIR instruments of SMHI and NASA are equipped with a YSI-thermistor for monitoring the dome temperature near its rim.

The pyrradiometer of the Middleton type, CN-1, is a radiation balance meter whose downward looking receiver surface is covered by a metallic cap. The temperature of the cap is measured and taken for the body temperature T_B in the evaluation formula. The thin poly-ethylene dome protecting the upward looking receiver surface must be continuously inflated with dry compressed air.

The "Schulze" pyrradiometer is represented by the upper sensor of the homonymous radiation balance meter manufactured by Dr. B. Lange, Berlin. This instrument is the only one of the participating sensors with a platinum resistance thermometer for measuring the body temperature T_B. For both pyrradiometers, the CM11 pyranometer listed on Table 1 delivers the global solar radiation signals needed for the evaluation.

All ventilation systems are attached to the side of the pyrgeometers with the exception of the AES device, the ventilator of which is placed at the bottom of the pyrgeometer. In the case of the MOH radiometers, the ventilated air is first blown into the body case and then streams forth to the dome. Three of the participating longwave radiometers are not ventilated.

2.2 Site and installation

The comparison was performed at Meteorologisches Observatorium Hamburg of Deutscher Wetterdienst. The observatory is located at 53°39'N, 10°07'E, 49 m above m.s.l. in a north-eastern suburb consisting of small residential houses and large garden areas.

The radiometers were installed on the measuring field on the roof of the observatory sufficiently far apart so that interferences were negligible and the horizon was free of obstructions according to WMO recommendations. Fig. 1 schematically shows the sturdy instrument carrier and the positions of the participating instruments, Fig. 2 is a photograph of the carrier with the instruments installed. The data acquisition system was located inside the building. The length of the measuring cables was about 25 m.

group	owner	country	type	no.	temperature sensor body T_B	temperature sensor dome T_D	ventilation system	formula for first evaluation of atmospheric rad. A	remarks
Pyrgeom.	AES	Canada	PIR(Ep.)	12120	YSI44031	–	type NARC	$A=V/R_L+\sigma \cdot T_B^4-0.026 \cdot G$	
	EKO	Japan	MS-200	S88047.3	YSI44031	–	type EKO	$A=V/R_L+\sigma \cdot T_B^4-0.055 \cdot G$	
	MOH	Germany	PIR(Ep.)	26095 F3	YSI44031	–	type MOH	$A=V/R_L+\sigma \cdot T_B^4-0.026 \cdot G$	
	NASA	USA	PIR(Ep.)	26181F3	YSI44031	YSI44031	–	$A=V/R_L+\sigma \cdot T_B^4-4 \cdot \sigma \cdot (T_D^4-T_B^4)$	
	SMHI	Sweden	PIR(Ep.)	27184 F3	YSI44031	YSI44031	type SMHI	$A=V/R_L+\sigma \cdot T_B^4$	shaded by sun-following disk from 7 Oct 1989 to 2 April 1990
	MRF	U.K.	PIR-Foot	H127	YSI44211	–	–		
Pyrrad.	AES		CN-1	659-X	YSI44031	–	–	$A=V/R_L+\sigma \cdot T_B^4-G \cdot R_S/R_L$	lower side of sensor covered by a cap
	MOH		"Schulze"	755	Pt-100	–	type MOH (Lange)	$A=V/R_L+\sigma \cdot T_B^4-G \cdot R_S/R_L$	lower sensor covered by a cap
Pyranom.	MOH		CM11	88 2043	–	–	type MOH		for measuring G

V: mV-signal

R_L: longwave responsivity

R_S: shortwave responsivity

G: global irradiance (W/m^2)

Table 1: Participating instruments

2.3 Schedule and weather

The comparison was held during the ten months from July 1989 to April 1990. The major actions during the comparison were:

1989,	10 to 19 July:	Installation and test phase
	20 July (0000 UTC):	Start of the comparison measurements
	17 August:	EKO pyrgeometer model MS-200: start of measurement (due to late delivery)
	11 to 12 September:	PIR-Foot (MRF): replacement of the thermistor in the body
	07 October:	PIR (SMHI) equipped with a sun-following shade-disk (9.6°) of MOH
	22 November to 14 December:	PIR (AES) equipped with the ventilation device of MOH. PIR (MOH) without ventilation from now on
1990,	05 April:	Pyrradiometer (MOH) replaced by Pyrradiometer "EXP"
	12 April:	PIR (SMHI) without shade-disk from now on
	17 April (1043 UTC):	End of comparison measurements
	April to July:	Indoor calibration of radiometers

The climate of Hamburg is maritime; that means moderate seasonal variations of temperature, rare calm situations and a strong variablility of cloudiness. The weather conditions during the period are summarized in Fig. 3 which shows the seasonal variations of temperature, humidity, precipitation and relative global solar radiation. The winter 1989/90 was very mild.

2.4 Data acquisition

The signals of 20 sensors, a constant resistor, and a short circuit had to be recorded. The latter two were used for checking the performance and stability of the multimeters. The sensors were connected to three 10-channel-multimeters (model PREMA 5000 and 5001) which were controlled by a Commodore 610 computer. A line printer and a floppy disk were used for data presentation and storage (see Fig. 4).

The sampling rate was one reading (of every sensor) every 30 seconds. The three multimeters were switched almost simultaneously so that sensors belonging to the same instrument were sampled almost simultaneously (see Fig. 5). About 12 seconds were needed to read all channels.

The raw data (mV, kΩ) were stored on disk together with date/time referred to UTC. They were also converted to physical units (mW/cm², degC) using preliminary calibration constants, and displayed on screen for quick reference. Every hour, that is every 120 cycles of reading, an hourly sum or average was calculated and printed (see example in Fig. 6). Every day about 0.8 MByte of data were written on disk. About 220 MByte of raw data were produced during the whole comparison.

Whereas the raw data have a time resolution suitable for short-term variation analysis, the evaluation was mainly based on halfhourly sums which are most suited for standard applications in solar energy engineering and collector testing.

3. EVALUATION METHOD

3.1 General

According to the objectives of the comparison, the main quantity to be compared was the downwelling longwave atmospheric radiation A, as received on the horizontal plane. Further, the dependence of measured A-values on the accuracy of responsivities and correction factors was investigated, and methods of adjusting the measured values were explored; these investigations were computer experiments executed with the raw data. Finally, a comparison of radiometer temperatures was performed to derive possible explanations of the differences between the measured A-values.

The atmospheric radiation A was derived from the quantities

- radiometer output V,
- temperatures T_B and T_D of radiometer body and dome, respectively,
- longwave and shortwave responsivities R_L and R_S respectively, of the radiometer,
- global solar radiation G

with the help of the formula

$$A = V/R_L + \epsilon \cdot \sigma \cdot T_B^4 - k \cdot \sigma \cdot (T_D^4 - T_B^4) - c \cdot G. \quad (1)$$

For pyrradiometers, c equals R_S/R_L; for pyrgeometers, $c < 0.1$. k is a correction factor estimated < 5 which is set zero if the dome temperature T_D is not measured. The emittance ϵ is usually assumed to be 1. The values recommended by the instrument owners of k and c can be taken from Table 1, column 8.

3.2 Software

Software was written to produce the following tables:

- Basic tables of halfhourly sums of A for each day. The parameters in eq. (1) to calculate the absolute A-values in $J \cdot cm^{-2}$ can be set to meet any special requirement. Relative values can be derived from mean values of each desired group of the participating radiometers.

- Monthly tables of daily sums of A, including ten-day and monthly mean values and the monthly standard deviation.

- Monthly tables of A-sums over specified sections of a day.

- Monthly tables of A-sums within a specified energy interval.

- Monthly tables of A-sums selected according to specified intervals of air temperature or other meteorological quantities.

Additional software was written to graphically display the seasonal and diurnal variations of the A-values.

4. COMPARISON OF ATMOSPHERIC RADIATION A

4.1 Classification of meteorological conditions

The meteorological conditions affecting atmospheric radiation A may be divided in 4 groups with increasing requirements on radiometer performance; T_A is the air temperature:

Type I: Night and overcast sky with thick low cloud layer:

Since G = 0, V very small and $T_D \approx T_B \approx T_A$, it follows

$$A \approx \epsilon \cdot \sigma \cdot T_B^4.$$

Type II: Day and overcast sky with low cloud layer:

Under thick clouds, G and V are very small and $T_D \approx T_B \approx T_A$, consequently

$$A \approx \epsilon \cdot \sigma \cdot T_B^4.$$

When the cloud layer is not thick, still $T_D \approx T_B \approx T_A$, consequently

$$A \approx V/R_L + \epsilon \cdot \sigma \cdot T_B^4 - c \cdot G.$$

Type III: Night and sky temperature $< T_B$, e.g. clear sky and low water vapor content:

$$A \approx V/R_L + \epsilon \cdot \sigma \cdot T_B^4 - k \cdot \sigma \cdot (T_D^4 - T_B^4).$$

Type IV: Sunny day. All terms in eq. (1) are to be considered.

The more terms considered in eq. (1), the less accurate are the A-values, in general. Further, the data from the non-ventilated radiometers are expected to be less accurate because of possible deposition of dew or rime on the dome.

4.2 Diurnal cycles of halfhourly sums

In the following, the diurnal cycles of measured halfhourly A-sums on selected days are presented. The days are selected according to typical weather conditions which affect the accuracy of the measured A-values.

Fig. 7 shows the daily curves of all radiometers on the nearly cloudless 29 March 1990. The curves are labeled by the channel number of the respective radiometer. Type I conditions are observed shortly after midnight with a small spread of about 2 % of the curves. Type III conditions prevail in the early morning and late evening and include two peaks caused by clouds; the spread between the curves amounts to about 5 %. The single morning peak observed at the non-ventilated AES-pyrradiometer may be caused by dew deposited on the dome. The largest spread, up to 13 %, occurs - as expected - under type IV conditions, increasing with increasing solar radiation. The values of the EKO pyrgeometer are generally the highest and show two "solar peaks" which are caused by small scratches in the filter of the dome near its foot; the scratches are transparent for the solar beam at low angles of incidence. The values of the AES pyrgeometer are the lowest.

Fig. 8 shows the daily curves of 23 November 1989. After a clear night (type III conditions), a sunny morning arises (change to type IV) with a short "cloud peak" in between. The spread amounts to about 5 %. The approach of a cloud system after 10 UTC induces a steep increase by nearly 20 $J \cdot cm^{-2}$, reaching 60 $J \cdot cm^{-2}$ under overcast skies (type III) and a corresponding small spread of about 2 % for the rest of the day.

Fig. 9 shows the effect of rime on the cold and mostly cloudless 29 November. The curves with even numbers belong to those radiometers which were not ventilated on this day. The A-values are around 50 $J \cdot cm^{-2}$ in the early morning, 25 % more than expected, because of rime on the domes. The MOH pyrradiometer also has a "rime peak" around 06 UTC, indicating that the non-heated air stream is not sufficient for thawing under winter conditions. After cleaning in the morning, rime continues to form until the relative humidity has decreased. During the late evening hours, the rime effect is observed again, but to a smaller extent because of increasing cloudiness.

Fig. 10 shows the curves of the very foggy 12 December which starts with a clear sky and the above-mentioned rime effect at midnight. The spread of the curves, with the exception of the EKO pyrgeometer, is generally less than 2 %, as expected under ideal type II and type III conditions. During the noon hours, the fog is lifting and consequently the spread increases to about 4 %.

Fig. 11 shows the curves of the rainy 7 March. The wind speed is small (< 1.5 m/s) and the cloud base is low. Type I and II conditions are realized with the exception of a "cloud hole" around 21 UTC. Again, the values of the EKO pyrgeometer are enhanced. The morning values of the MOH pyrradiometer are somewhat lower than those of the other radiometers; possibly the dome was cooled by ventilation-enforced evaporation of droplets. The spread of the other curves is less than 2 %.

Fig. 12 shows the curves of the very stormy 26 February (maximum wind speed at noon: 18 m/s). As a consequence, the temperatures of body and dome of all radiometers are almost equal. Structure and level of the curves can be explained by the passage of a cold front at noon and the change of cloudiness thereafter. During both halves of the night, the spread of the curves is about 3 to 4 %. As expected, the spread of the minima is larger than that of the maxima. At some hours, the spread of the curves is within 2 % as under ideal type I conditions.

4.3 Seasonal variation of daily sums

The daily sums are equivalent to the average of 48 halfhourly sums. Therefore, an assignment of types of meteorological conditions is not possible. Particularly, the characteristics of type IV are smoothed by summing the day and night values.

In order to facilitate a survey on the data, the percent deviations of the daily sums measured by each instrument from the daily sums of the SMHI pyrgeometer have been computed. This instrument is chosen as a reference because it is ventilated and equipped with temperature sensors at the body and the dome and, since 4 October, with a shade-disk to prevent direct solar radiation from reaching the dome. The shade-angle 9.6° covers 0.3 % of the hemisphere and therefore has negligible effect on the received hemispherical longwave radiation A. The reference values measured before 4 October have been corrected for global solar radiation effects by the term $0.026 \cdot G$.

Fig. 13 shows the results for all pyrgeometers of the Eppley Type PIR. The absolute reference values (right scale) are between 3250 J · cm^{-2} in summer and 2000 J · cm^{-2} in late fall with monthly variations > 500 J · cm^{-2}.

The values of the MOH pyrgeometer deviate from the reference values generally less than about ±1 % with the exception of the period without ventilation (22 November to 14 December) during which deviations up to 5 % occur due to rime or dew.

The values of the NASA pyrgeometer deviate from the reference by an offset of about +1 % and larger peaks up to about 7 %. The latter may be caused by rime and dew, the former by an imperfect correction for the solar heating effect by the k-factor; Fig. 14 shows an improved curve which has been derived for k = 0 and c = 0.026.

The deviations of the AES pyrgeometer show a decreasing negative offset ranging from about -2.5 % in summer to -1 % around 1 January, followed by an increasing trend to about -2.5 % at the end of March. The replacement of the ventilation system by one of the MOH type during the period from 22 November to 14 December leads to 1 % smaller offsets. Generally, the fluctuations of the curve do not exceed 2 %.

Fig. 15 shows the deviations of the remaining two pyrgeometers. The curve for of the PIR-Foot does not have any offset trend. The deviations of the minima are within ±1 %. The positive fluctuations are generally < 2.5 %. Some peaks exceed 2.5 % synchronously with the strong peaks of the deviation curve for the EKO pyrgeometer. Since the PIR-Foot pyrgeometer is not ventilated and its output is not corrected for global solar radiation, the maxima mentioned may be caused by rime and dew or by solar radiation, or by both.

The offset of the EKO pyrgeometer is around +2 %. The maximum fluctuations go up to 8 %; they generally show up on sunny days and can be attributed to "solar effects" as in Fig. 7.

Fig.16 shows the curves of the deviations of the pyrradiometer values. The curve for the AES pyrradiometer has a summer offset of about +2 % which decreases during fall to 0 %. In later periods, with frequent dew and rime, the offset increases again with maxima of more than 5 %.

The curve for the MOH pyrradiometer exceeds the positive deviations of the AES pyrradiometer curve in July and August by about 3 %. After replacement of the dome and recalibration at the end of August, both curves are close together (±1 %). They deviate again in the period of frequent dew and rime because the AES pyrradiometer is not ventilated. In the winter months of 1990, the curve for the MOH pyrradiometer has an offset of about -1 % with an increasing trend in March. In the evaluation of the measurements, continuous ageing of the dome was assumed and accounted for by a time variation of the calibration factor.

4.4 Seasonal variation of ten-day means of daily sums

Ten-day means of daily A-sums show the seasonal trends clearer than the individual daily sums. The curves for all radiometers are displayed in Fig. 17. The steep minima around 2250 $J \cdot cm^{-2}$ in the second ten-day period of November can be explained by a sequence of clear days with low humidity as well as by the unusually high temperatures for the winter months. Fig. 18 shows the corresponding curves restricted to A-values between 0930 and 1330 UTC in order to demonstrate the influence of global radiation around noon.

The spread between the curves can be better illustrated by means of relative values which have been normalized to the values measured by the SMHI pyrgeometer used as a reference. Fig. 19 shows the normalized curves corresponding to Fig. 17. The spread of the curves is about 4 % if the values of the EKO pyrgeometer are not considered. The deviations of most curves are between 0 % and 2 %. The values of the AES pyrgeometer, however, are 2 % lower than the reference values, before the last ten-day period of November; after replacement of the ventilating system, the deviations are smaller than -1 % over 60 days, but then increase to -2 % at the end of March. The values of the MOH pyrradiometer increase to a maximum deviation of +3 % in August.

The normalized curves in Fig. 20, which correspond to Fig. 18, show strong deviations up to 9 % for the MOH pyrradiometer during the summer months and the "solar peak" effect for the EKO pyrgeometer. For the AES pyrgeometer, negative deviations of around -4 % exist; they are reduced to about -1.5 % during the dark winter months. Often, weak minima occur simultaneously with the above-mentioned "solar peaks". The smallest deviations of ± 1.5 % exist for the PIR-Foot and MOH pyrgeometers and for the AES pyrradiometer.

Fig. 21 shows the normalized ten-day means of the A-sums from 18 to 24 UTC (first half of the night). The deviations of nearly all values are between 0 % and 3 % with peaks in the first ten-day period of December. The values of the AES pyrgeometer, however, are negative.

Fig. 22 shows the corresponding curves for the hours between 00 and 06 UTC (second half of the night) in which dew and rime occur more frequently. The difference between Fig. 21 and 22 is small but the shift of the peak from December to November and October is remarkable.

4.5 Summary

The results of the comparison do not give information on the absolute accuracy of the measurements because a reference radiometer is not available at present. But the differences of the measuring values obtained with the various radiometers give information on the relative measuring uncertainty and on the lower limit of the absolute accuracy. Further, systematic errors of the radiometers can be detected.

The spread of the diurnal and seasonal variations of A-values measured by the various radiometers show typical variations which depend on the global solar radiation and on the amount of cloudiness.

Some deviations are obviously caused by not using a ventilation system for preventing dew or rime and a sun-following disk for shading the domes from direct solar radiation.

The differences of the measured values are largest when the sky is clear and the direct solar radiation is high. The lowest differences occur during a night with an overcast sky and thick cloud layers. As shown by examples, the difference of the measured values can increase up to 15 % around noon under clear sky conditions. At overcast night hours, the measured differences are generally lower than 3 %.

The spread of the seasonal curves over the total comparison period is lower than 8 % if the "solar peaks" of one instrument are not considered. Further, if the large differences are mitigated by technical measures, the remaining spread is lower than 5 %. For three pyrgeometers and one pyrradiometer, the spread of the seasonal variations is lower than 2.5 %.

The spread of the seasonal variations of the ten-day means of the daily sums is generally lower than 4 %. Most of the compared values are within 2 %. Exceptions exist with the AES pyrgeometer, the MOH pyrradiometer and the EKO pyrgeometer during certain times of the comparison period.

The ten-day means of the A-sums from 0930 till 1330 UTC are most disturbed by high global solar radiation around noon. For some instruments, the spread of the curves increases up to 15 %, but the majority of the instruments deviate by less than 4 %.

5. COMPARISON OF INSTRUMENT TEMPERATURES

5.1 Relation of measured values of A to body temperature T_B

The electrical sensor measuring the body temperature T_B is an essential part of pyrgeometers and pyrradiometers because T_B has great influence on the measured value of the atmospheric radiation A. The body temperature T_B shall follow the air temperature T_A as closely as possible.

The strong correlation of T_B and A is demonstrated by Fig. 23 where all measured half-hourly sums of A are plotted versus the corresponding body temperatures T_B in steps of 2 K. The standard deviations are generally between 5 and 6 $J \cdot cm^{-2}$. The curves for the different radiometers run more or less parallel with a spread of only 2 to 3 $J \cdot cm^{-2}$. Exceptions are the curve of the MOH pyrradiometer which deviates towards higher A-values for $T_B \geq 21$ degC, and the curve of the AES-pyrgeometer which deviates towards lower values for $T_B \geq 9$ degC. The maximum difference between both curves is about 8 $J \cdot cm^{-2}$. The drop of the curves at about -4 degC can be explained by the decrease of cloudiness.

Figs. 24 and 25 show plots of the A-values versus T_B separately for daytime and nighttime. Particularly the daytime values exhibit larger variations. The plot for the AES pyrgeometer deviates from those of the other instruments.

Of two pyrgeometers of the PIR-type, the temperature of the rim of the dome, T_D, has been measured. T_D was used to correct for the absorption effect of the silicon dome. This correction is approximate since the rim temperature does not exactly represent the effective dome temperature.

The temperature sensors of the pyrgeometers and of the AES pyrradiometer are thermistors of the same type, the measured resistances R of which have been converted to temperature by means of the formula

$$T = (2.339\text{-}R)/0.01799 + 0.008 \cdot (2.339\text{-}R)/0.01799 - 10.$$

The temperature sensor of the MOH pyrradiometer is a Pt-100 resistance thermometer which has been operated with a constant current of 1.0 mA. The temperature has been calculated by the formula

$$T = (R\text{-}100)/0.389 - 0.100.$$

In the forgoing equations, T is in degC and R in kΩ.

Before 1 December, the ambient air temperature T_A has been measured by a Pt-100 resistance thermometer in a Baumbach screen which may read too high by some tenths of a degree when exposed to bright sunshine. Later on, a Frankenberger thermometer which has a precision of 0.1 K was used.

5.2 Difference between body temperature T_B and air temperature T_A

Fig. 26 shows the seasonal variation of the ten-day means of $\Delta T_{BA} = T_B - T_A$ for each radiometer. The general trend of all curves is an increase of ΔT_{BA} to the maximum in mid-August and then a decrease until the first ten-day period of December followed by a smooth increase until April. This trend may be explained by the fact that the temperatures of the radiometers and of the ambient air are influenced by radiative heat exchange.

The ventilated air stream may influence the instrument temperature more or less depending on the used ventilation system. For instance, the ΔT_{BA}-values of the AES pyrgeometer exceed the mean values of the other radiometers by 1.5 K to 2 K. The 20 W-ventilator is installed beneath the pyrgeometer and first heats its body and afterwards the dome. During the period 22 November to 14 December, the instrument has been equipped with the MOH ventilation system which merely consumes 6 W and protects the body of the pyrgeometer from the ventilated air. During this period, ΔT_{BA} of this pyrgeometer is close to that of the other radiometers.

The ΔT_{BA}-values of the non-ventilated radiometers (No. 2, 4, 8) are always the lower ones, with a spread of the curves $\leq$ 0.5 K. The replacement of the temperature sensor of the PIR-Foot in September does not cause any significant step in the curve. The ΔT_{BA}-curve of the ventilated EKO pyrgeometer lies generally above the mean of the other curves by about +1 K. The ΔT_{BA}-curve of the MOH pyrradiometer is remarkably high since the second ten-day period of January as the ventilated air has been electrically heated from that time on.

Fig. 27 demonstrates the effect of strong winds on the diurnal cycle of T_B on 26 February. The body temperatures of the non-ventilated instruments are very close to T_A ($\Delta T_{BA} \leq 0.3$ K) at the time of maximum wind speed. The T_B-values of the AES pyrgeometer deviate from T_A by +1 K to +2 K.

The correlation between the halfhourly mean values of T_B and T_A of the total period is displayed in Fig. 28. The intersection of the regression line is positive for the AES pyrgeometer, whereas it is negative for the AES pyrradiometer and almost zero for the SMHI pyrgeometer. The scattering of points around the regression line is relatively small for the SMHI pyrgeometer. The diagram for the AES pyrgeometer shows a separated linear array of points between -7 degC and 10 degC which belongs to the period when the MOH-ventilation was used.

5.3 Difference between body temperature T_B and dome temperature T_D

Fig. 29 shows the seasonal variation of the ten-day means of the difference $\Delta T_{BD} = T_B - T_D$ for the ventilated SMHI and the non-ventilated NASA pyrgeometers. In case of the former pyrgeometer, ΔT_{BD} is -0.1 K in the periods without dome-shading; that means the dome is warmer than the body. Afterwards, ΔT_{BD} fluctuates between 0 and 0.1 K. In case of the non-ventilated NASA pyrgeometer, ΔT_{BD} is 0.1 K till October and then varies between 0.2 K and 0.1 K with a single maximum of 0.3 K. On the average, the temperature differences are on the order of magnitude of the measurement uncertainty.

Fig. 30 shows the diurnal cycle of ΔT_{BD} for both pyrgeometers on the sunny days 19 August and 29 March. On the August day, the ventilated but unshaded SMHI pyrgeometer has a minimum ΔT_{BD} of -0.8 K at 11 UTC and maxima during the night of +0.2 K. As expected, the non-ventilated NASA pyrgeometer has a smaller minimum of -0.2 K at 11 UTC and a night maximum of +0.3 K. On 29 March, the SMHI pyrgeometer dome is shaded so that around noon a maximum of 0.4 K occurs, indicating that the dome is cooler than the body. The NASA pyrgeometer curve shows a broad relative minimum of 0.0 K around noon.

5.4 Summary

For each radiometer, the mean values of the halfhourly A-sums constitute a monotonously increasing function of the body temperature. The differences between the means of A recorded by different radiometers are generally less than 3 $J \cdot cm^{-2}$.

The ten-day mean of the difference between the body temperature and the ambient air temperature is generally between -1 K and +1 K, depending on the season and the ventilation system used. However, certain ventilation systems may generate temperature differences up to 3 K. Under stormy weather conditions, the differences are reduced.

The correlation between body temperature and air temperature is markedly different in case of some radiometers.

On the ten-day average, the difference between body temperature and dome temperature of PIR pyrgeometers is small ($\approx$ 0.1 to 0.2 K). On sunny days, significant diurnal cycles occur with an amplitude of up to $\pm$1 K, depending on ventilation and shading.

6. COMPARISON OF CALIBRATION RESULTS

6.1 General

For determining the atmospheric radiation A from the radiometer signal, the longwave responsivity R_L and, if pyrradiometers are used, additionally the shortwave responsivity R_s have to be known. The accuracy of these calibration factors strongly influence the uncertainty of the A-values, particularly under type IV conditions which are typical for solar collector tests. The comparison of calibration factors derived by different laboratories may help to understand the differences of the measured A-values.

The following laboratories have participated in the calibration of the radiometers: NARC of the Atmospheric Environment Service (Canada), MOH of Deutscher Wetterdienst (Germany) as well as the radiometer manufacturers Eppley Laboratories (USA) and EKO Instruments Trading Co. (Japan). The longwave calibration procedures are based on the use of blackbody radiators. For the shortwave calibration, generally lamps as well as reference radiometers which have been calibrated outdoors by comparison with standard pyrheliometers under clear sky conditions, have been used.

6.2 Pyrgeometers

Fig. 31 presents a compilation of the measured longwave responsivities of the 6 pyrgeometers. As indicated by symbols, the NARC values result from the "blackbody method" and the "sphere cooling method", the MOH values from the "warm blackbody method" and the "melting iceblock method".

The MOH results are higher than the other in all cases with the exception of the responsivities obtained with the "sphere cooling method". The differences, in percent, between the longwave responsivities determined by MOH and NARC and by MOH and the manufacturer, respectively, are:

	NASA	AES	SMHI	MOH	EKO
MOH-NARC	9	4	15	7	7
MOH-Manufacturer	11	-	13	3	4

6.3 Pyrradiometers

Only for the AES pyrradiometer of the Middleton type CN-1, two sets of calibration results obtained by NARC and MOH are available. The following shortwave and longwave responsivities R_S and R_L, in $\mu V/W \cdot m^{-2}$, have been measured:

	R_S	R_L
NARC (1989)	42.6	40.7
MOH (Aug. 1989)	44.0	44.6
MOH (Juni 1990)	42.9	46.7

The R_S-values determined by MOH and NARC deviate within 3%, the R_L-values by 10 %. The increase of R_L after 10 months exposure in the field is unexpected since dome ageing usually reduces the responsivity.

6.4 Summary

The uncertainty of the responsivity determined by calibration has a strong influence on the accuracy of the derived hourly A-values on sunny days.

The differences of the longwave responsivities determined by the calibration methods of NARC and MOH are in the range 4 to 15 %. The MOH-values are always higher than the results obtained by the manufacturers (Eppley 3 to 13 %, EKO 4 %).

The shortwave responsivities determined by the calibration methods of NARC and MOH deviate within 3 % in case of the AES pyrradiometer.

One of the main reasons for the differences in the longwave responsivities may be the thermal gradient in the radiometer which effects the different calibration procedures to a different extent.

7. COMPUTER SIMULATIONS

7.1 General

In order to investigate the influence of the calibration factors on the measured values of atmospheric radiation A, the calibration factors as given by the owners of the radiometers have been varied within certain limits, and the resulting A-values have been computed. Further, by means of computer algorithms, selected diurnal cycles of measured A-values have been adjusted to the diurnal cycle of the A-values of one radiometer which has been taken as a reference.

In case the number of adjustment factors and halfhourly A-values required for obtaining a good fit turns out to be small, one can assume that simple systematic errors of the calibration procedure are the source of the deviating measured values. The assumption holds even more if the adjustment factors derived for one specific day turn out to be applicable to other days.

7.2 Variation of the longwave and shortwave responsivities, R_L and R_S

To cover the whole range of observed discrepancies of the calibration factors, R_L has been varied by ± 20 % in steps of 5 %, and R_S has been varied by ± 4 % in steps of 1 % with respect to the values given by the owners of the radiometers.

Fig. 32 demonstrates the influence of R_L-variations on the diurnal cycle of the measured values A of the NASA pyrgeometer on 29 March. Negative variation steps lead to progressively increasing, positive variation steps to decreasing A-values. At noon, the largest effects are observed: variation of R_L by -15 % induces a decrease of A by 7 %; variation of R_L by +15 % leads to 5 % higher values of A. Similar results are obtained for the clear second-half of the night. R_L variations of ± 5 % give ± 2 % variation of A at noon and about ± 1.5 % during the clear night.

The behaviour of the AES pyrradiometer on 29 March is slightly different, see Fig. 33. When R_L is varied by ± 15 %, A varies by +8 % and -12 %, respectively, at noon, and by +3 % and -6 % at clear night. Variations of R_L by ± 5 % result in changes of A by ± 3 % at noon, by ± 1.5 % at clear night.

Fig. 34 shows the effect of R_L variations on the seasonal cycle of the ten-day means of daily A-sums for the NASA pyrgeometer. ± 15 % variation of R_L results in +2 % and -3 % deviations of the curve if the peaks are not considered. At the peaks, the spread is from +4 % to -5 %.

Fig. 35 shows the effect of R_S-variations on the diurnal cycle of A-values recorded by the AES pyrradiometer on 29 March. The variation effect is approximately linear. ± 4 % variation of R_S results in ± 10 % deviation of A. That means the uncertainty of R_S is four times more effective on A than that of R_L.

7.3 Variation of the correction factors k and c

Fig. 36 shows the effect of varying the factor k on the diurnal cycle of A recorded by the NASA pyrgeometer on 29 March. The corresponding A deviations are between 0 % at 14 UTC and 5 % at 19 UTC for $k \leq 8$. Mostly, the body temperature T_B is higher than the dome temperature T_D so that an increase of k results in an increase of A. When the dome is heated by direct solar radiation, T_D is higher than T_B and A decreases with increasing k, as in the time interval 8 to 13 UTC. The corrections of A produced by $k = 8$ and $k = 4$ amount to 1 and 0.5 $J \cdot cm^{-2}$, respectively.

Fig. 37 shows the effect of a variation of k on the ten-day means of daily sums of A recorded by the NASA pyrgeometer. The corresponding variations of A are smallest in the summer months. They always increase with increasing k. $k = 4$ as used during the comparison measurements results in an 1 to 2 % increase of A during the winter halfyear.

Fig. 38 demonstrates the effect of varying the factor c which shall correct for global solar radiation interference, on the diurnal cycle of the A-values recorded by the AES pyrgeometer. Corrections with $c = 0.05$ and 0.025 reduce the atmospheric radiation A by 10 and 5 %, respectively, at noontime. In case of the shaded SMHI pyrgeometer, $c = 0$ i.e. no correction gives the best fit, see Fig. 39.

Fig. 40 illustrates the influence of the factor c on the measured values of the unshaded SMHI pyrgeometer on 21 September which is a day with advection of warm air and increasing turbidity. The correction with $c = 0.05$ reduces A by about 5 %.

The influence of varying c on the ten-day means of the daily sums of A recorded by the MOH pyrgeometer is illustrated by Fig. 41. As the daily sums of A comprise the night when global solar radiation is zero, the effect of c which shall correct for global solar radiation is small; $c = 0.05$ changes A by 2.5 % at most.

7.4 Method of adjusting measured A-values to reference values

The halfhourly sums of atmospheric radiation recorded by the SMHI pyrgeometer are taken as reference values. For the adjustment, the longwave responsivity R_L and the correction factor c of the radiometers are used. The adjustment is performed for the day 29 March during which type IV weather conditions were present.

For the adjustment by means of R_L, the two halfhours 0200 - 0230 and 2230 - 2300 UTC are taken because there were not any cloudiness and dew observed during these times. The longwave responsivity R_L as given by the owner of the radiometer is multiplied by an adjustment factor K_L which is computed by means of an equation analogous to eq. (1):

$$A_{ref} = V/(K_L \cdot R_L) + \sigma \cdot T_B^4 - k \cdot \sigma \cdot (T_D^4 - T_B^4) - c \cdot G \qquad (2)$$

where A_{ref} is the halfhourly sum of the atmospheric radiation measured by the reference pyrgeometer. Eq. (2) yields two values K_L, one for each of the halfhours mentioned above; the arithmetic mean is called $\overline{K}_L$.

For the adjustment by means of c, the halfhourly sum 1100 - 1130 UTC is taken, and an adjustment factor K_c is computed according to

$$A_{ref} = V/(\overline{K}_L \cdot R_L) + \sigma \cdot T_B^4 - k \cdot \sigma (T_D^4 - T_B^4) - c \cdot K_c \cdot G. \quad (3)$$

When the input parameters k and c are unknown, the values $k = 0$ and $c = 0.026$ are assigned to the radiometer. The resulting adjustment factors $\overline{K}_L$ and K_c for each radiometer are compiled on Table 2.

Table 2: Adjustment factors $\overline{K}_L$ (for R_L) and K_c (for c)

Radiometer		c	$\overline{K}_L$	K_c
NASA	PIR	0.026 (fictitious)	0.960	1.300
AES	PIR	0.026	1.027	0.418
MOH	PIR	0.026	0.950	0.958
EKO	Pyrgeom.	0.055	0.875	1.130
MRF	Foot-PIR	0.026 (fictitious)	0.944	0.437
AES	Pyrrad.	1.046	0.916	0.969
MOH	Pyrrad.	1.042	0.963	1.015

7.5 Results obtained with the adjustment method

Fig. 42 presents the diurnal cycle of halfhourly A-sums on 29 March 1990, generated with the adjustment method. From the curves, the following conclusions are drawn:

- The A-curves of all four PIR pyrgeometers coincide within 1 %.
- The apparent maxima which are caused by dew or direct solar radiation, are generally not diminished by the adjustment.
- The A-curves of the two pyrradiometers deviate from the curves of the PIR pyrgeometers distinctly during the sunny hours.
- The A-curve of the Foot-PIR exhibits two maxima of about 4 % in the morning hours. The reason is unknown.
- During the undisturbed night hours, the adjustment makes the A-curves of all radiometers to coincide within 1 %.

The adjustment factors derived from the data of 29 March have also been applied to the data of the sunny 23 February. From Fig. 43 one learns:

- The spread of the A-curves of the PIR pyrgeometers is generally $\leq$ 2 %.

- With the exception of the MOH pyrradiometer, the curves of all instruments deviate by less than 2 % during the night hours.

- The curves of the pyrradiometers show a wider spread up to almost 5 % during the sunny part of the day. The Foot-PIR exhibits a short-time deviation of about 4 % in the forenoon.

Fig. 44 shows the results of the adjustment applied to the data of the sunny 22 October:

- The spread of the A-curves of the PIR pyrgeometers does not surpass 2.5 %.

- The A-curves of the pyrradiometers deviate from the A-curves of the PIR pyrgeometers by up to 5 % at noon.

- During the second half of the night, all curves coincide within 1.5 %.

For comparison, Fig. 45 shows the not-adjusted curves which exhibit a considerable spread particularly at night.

The foregoing examples demonstrate that the adjustment method is capable of improving the measured data. Therefore, all halfhourly sums of atmospheric radiation measured during the comparison period are now adjusted by means of the appropriate $\overline{K}_L$ and K_c according to Table 2.

The adjusted halfhourly sums are integrated to daily sums and then averaged over ten-day periods, see Fig. 46. By comparing the curves of this Figure with the not-adjusted curves in Fig. 19, the "focussing effect" of the adjustment method becomes evident. Particularly in case of the PIR pyrgeometers, the spread of the curves is decreased to 1.5 % if the ten-day periods at the end of the year which are disturbed by dew and rime deposits on the instruments are excluded. In case of the pyrradiometers, however, the "focussing effect" is visible in only a few ten-day periods. The curve for the SMHI pyrgeometer acting as a reference is plotted in absolute units; values before 7 October when this instrument was unshaded have been corrected by $0.026 \cdot G$, G being the global solar radiation.

Fig. 47 presents the results of a similar evaluation. Instead of daily sums, now the time integral is taken over the 4 noon hours from 0930 to 1330 UTC. Comparing these curves with the corresponding but not-adjusted curves in Fig. 20 shows that the adjustment reduces the large deviations of the curves of the MOH pyrradiometer and of the EKO pyrgeometer but not of the AES pyrradiometer.

Analogously, Fig. 48 presents the adjusted curves in the case that the time integral is taken over the evening hours 1800 to 2400 UTC. Now, the curves of all radiometers exhibit a strong "focussing" due to the adjustment.

Similar results are obtained when instead of the SMHI pyrgeometer another pyrgeometer is used as a reference instrument.

7.6 Summary

Simulated variations of instrument responsivities and correction factors render insight into the dependence on these parameters of the measured atmospheric radiation data. The adjustment to reference values of the measured data gives hints to the causes of the differences between the data measured by different radiometers and thereby to the different measuring characteristics of the various radiometers.

Variations ΔR_L of the longwave responsivity R_L induce the following maximum variations, in percent, of halfhourly sums or of ten-day means of daily sums of measured atmospheric radiation if evidently erroneous data are excluded:

ΔR_L/%	pyrgeometer		pyrradiometer		pyrgeometer
	noon	clear night	noon	clear night	ten-day mean
−15.0	−7.0	−6.0	−12.0	−6.0	−3.0
+15.0	+5.0	+4.0	+8.0	+3.0	+2.0
−5.0	−2.0	−1.5	−3.0	−1.5	−1.0
+5.0	+2.0	+1.5	+3.0	+1.5	+1.0

In summary: A change by a certain percentage of the longwave responsivity R_L of the pyrgeometers leads to a maximum change of the measured A-value by half of that percentage at sunny noon, and by one fifth of that percentage on the ten-day average.

A change of the shortwave responsivity R_S of the AES pyrradiometer generates an inverse 2.5-fold percent variation of A at a sunny noon.

The effect of varying the correction factor k depends on the magnitude and sign of the temperature difference between dome and body of the pyrgeometer. For $k = 4$, the halfhourly A-sums may increase by +2.5 % at clear night. At a sunny noon, the induced negative deviation of A is small compared to the deviation produced by the correction factor $c = 0.026$. The ten-day means of the daily sums of A are generally increased when the correction factor k is applied; however, the increase is only 1 - 2 % for $k = 4$.

The correction by $c = 0.026$ may lead to 5 % decrease of A at a sunny noon in the summer halfyear. The numerical value chosen for c seems to be of the right order of magnitude because it produces rises of the A-records of the pyrgeometers at noon which are similar to the increase recorded by the sun-shaded SMHI pyrgeometer used as a reference.

The method of adjusting the measured A-values to those recorded by the SMHI pyrgeometer has proven effective. By means of the adjustment factors $\overline{K}_L$ and K_c determined for one single sunny day, the differences between the A-values recorded by different PIR pyrgeometers are reduced to 2.5 % during the whole measuring period. At night, the differences are even below 2 %. The ten-day means of the daily sums of A recorded by the PIR pyrgeometers generally differ by less than 1.5 %. In case of the pyrradiometers, the differences of the A-values at noon are reduced to 5 % or less. The adjustment method yields similar results when a pyrgeometer other than the SMHI instrument is taken as reference.

8. CONCLUSIONS

As mentioned in the introduction, the uncertainty of measuring the irradiance of hemispherical longwave radiation is on the order of ± 10 % at present. The comparison of measuring instruments reported here has shown that the measuring uncertainty of hourly irradiation of atmospheric radiation with simultaneous high global solar radiation is ± 10 % too. Under clouded sky and at night, the uncertainty is considerably less.

As measuring uncertainties of the pyrgeometric and pyrradiometric techniques have not indicated any systematic differences of the two measuring techniques, one can conclude that the differences between the outputs from the various instruments represent the measuring accuracies of the single instruments.

The main sources of the observed deviations of the measured values are the large differences of the calibration factors and correction factors determined by the various laboratories. This statement is corroborated by the strong dependence on these factors of the measured values, and by the success of the adjustment procedure based on one single adjustment being valid over the whole time of the comparison.

The large differences of the measured values at noon i.e. at high global solar radiation has been confirmed by the simulation calculations; variation of the short-wave responsivity has strongly come through to the measured values.

From the comparison of the longwave calibration procedures and of the measured values recorded by identical but differently calibrated instruments, one learns that the calibrating and measuring techniques for longwave radiation has to be more standardized than assumed to be necessary up to now. Possibly, different temperature gradients occuring in different calibration procedures are responsible for the deviating calibration results.

Several practical measures have been proven useful for avoiding or reducing measuring errors during the comparisons and are therefore recommended generally:

- Ventilation of the dome of the radiometer in order to avoid deposition of dew or rime and to bring the temperature of the dome to the level of the air temperature, approximately; however, heating of the radiometer body has to be kept small.

- Use of a sun-following shade-disk for shading the pyrgeometer dome from direct solar radiation.

- Checking the pyrgeometer dome for spatial inhomogeneties of the transmittance by applying parallel shortwave radiation.

The first two recommendations have already been taken as rules for the measurement of atmospheric radiation within the Baseline Surface Radiation Network (BSRN) of the Word Meteorological Organization (WMO).

Based on the experience obtained during the comparisons, the ventilated and shaded pyrgeometer has the following advantages over other techniques of measuring atmospheric radiation:

- Only one instrument is needed.
- Ageing of the dome by solar irradiation is slow.
- The dome is mechanically sturdy, therefore it can be cleaned safely.
- As the dome is relatively small, a small shade-disk and a relatively short bearing arm are sufficient, and ventilation is easy.

Both the pyrgeometric and the pyrradiometric techniques are not perfect at present but need some improvements. The filter dome of the pyrgeometer needs to be optimized. In the pyrradiometric technique, the measuring characteristics of the pyranometer are to be harmonized with the measuring characteristics of the pyrradiometer.

In the future, the following tasks are to be tackled:

- Further investigations of the errors in the measuring techniques for longwave radiation like absorption in the dome, dependence on wavelength of the emittance of the "black" receiver, temperature gradient in the radiometer body, and others.
- Standardization of the calibration procedures.
- Improvement and test of radiometers with the aim of developing a reference instrument.

9. RECOMMENDATIONS FOR SOLAR COLLECTOR TESTS

9.1 General

Outdoor tests of solar collectors are generally performed under fine weather conditions when there are no or only a few clouds in the sky. In such a case, a flat collector receives relatively high global solar radiation and relatively low atmospheric radiation. These are most unfavorable conditions for the measurement of atmospheric radiation which therefore requires special effort.

A tilted collector not only receives atmospheric radiation but longwave radiation emitted by the earth surface. With increasing inclination, the atmospheric radiation is more and more received from sky segments close to the horizon, and the contribution from the earth surface increases. Both the sky near the horizon and the earth surface have effective radiation temperatures close to the ambient air temperature. Therefore, the demand on the measuring accuracy of the longwave radiometer is less than in case of a horizontal collector.

In laboratory tests with hot solar simulators, large heat fluxes exist so that the demand on the measuring technique for longwave radiation is as high as in the case of outdoor tests with intense global solar radiation.

9.2 Outdoor tests of horizontal collectors

Most horizontal collectors as used for the heating of swimming pools, for instance, do not have glass covers so that the energy loss of longwave radiation emitted to the sky may reach 15 % of the incident global solar radiation.

Mean values of the atmospheric radiation falling on the horizontal collector can be derived from the air temperature with the help of parameterization formulae. Actual values are to be measured by a pyrgeometer which is to be ventilated and shaded by a sun-following shade-disk. The measuring uncertainty of this system is below 7 % so that the longwave radiation loss can be determined with an uncertainty around 1 % of the incident global solar radiation.

9.3 Outdoor tests of tilted collectors

Most inclined collectors are glass-covered whereby the heat losses by longwave radiation are appreciably reduced.

Since the spatial distribution of the longwave radiation emitted from the earth surface is often inhomogeneous, the radiometer is to be placed as close to the collector as possible. In case of large collectors, the variation of the longwave radiation at the edges of the collector should be measured. The radiometer recommended is a ventilated pyrgeometer but without a shade-disk in this case because the disk might interfere with the solar radiation to be received by the collector.

9.4 Laboratory tests

Solar simulators for testing large area collectors usually consist of a matrix array of medium-collimated shortwave radiation sources. Therefore, it is rather difficult to shade the pyrgeometer from the shortwave radiation emitted by the simulator lamps. The pyrgeometer is also to be protected from the intense longwave radiation of the hot simulator lamps. Further, it is still an open question whether the value of the longwave radiation measured at the rim of the collector is representative for the whole collector area.

Additional uncertainties arise when the major part of longwave radiation is received at small angles of incidence whereas the calibration of the pyrgeometer has been performed with hemispherical longwave radiation.

In any case, the pyrgeometer is to be ventilated. The overall measuring uncertainty depends on the configuration of the collector test stand and is to be determined by site-specific tests.

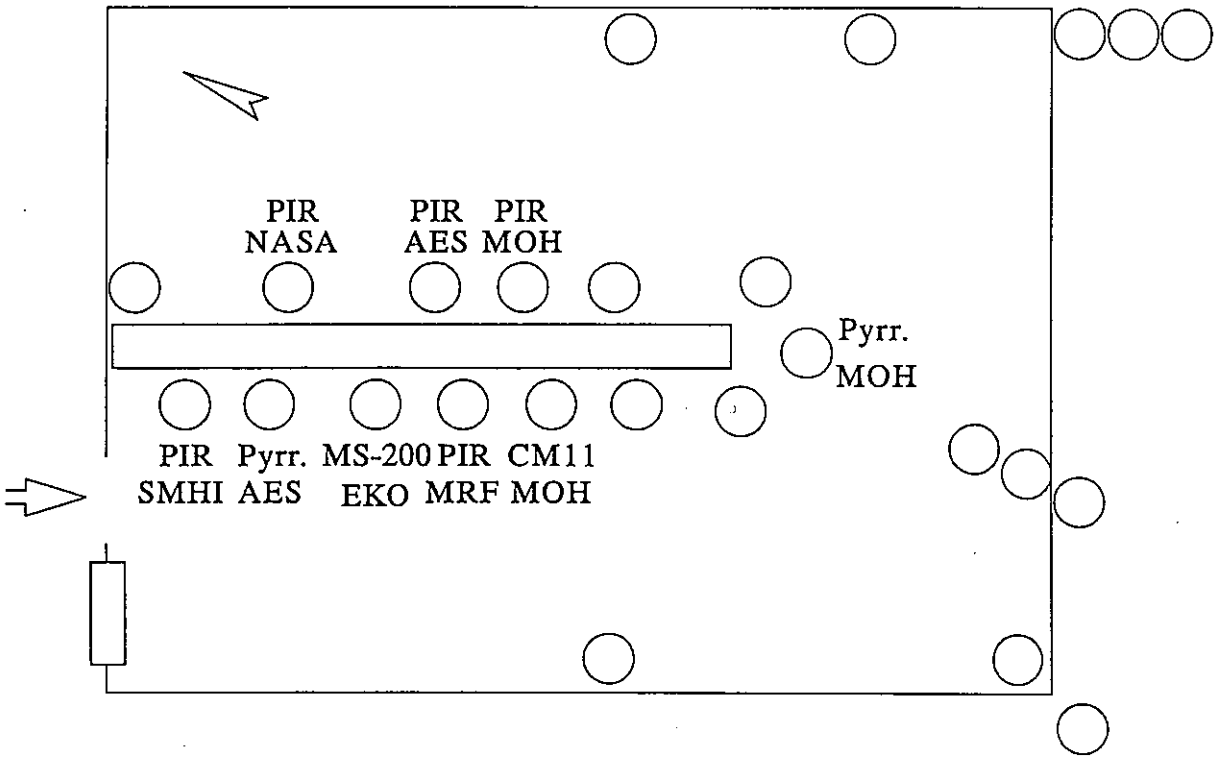

Fig. 1: Array of the instruments mounted at the carrier on the roof of the observatory (schematic)

Fig. 2: View of the central instrument carrier with instruments mounted

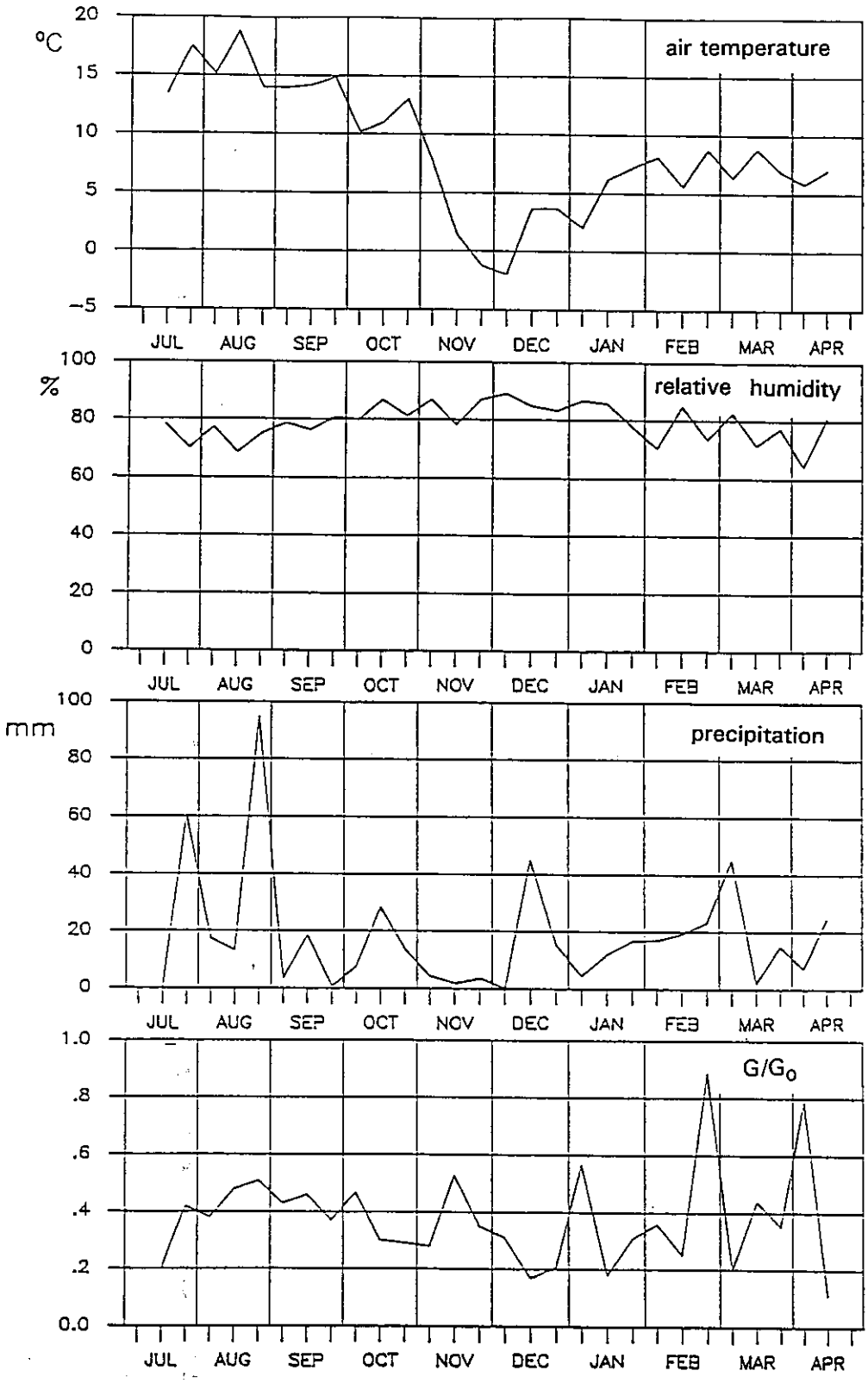

Fig. 3: Weather conditions during the comparisons

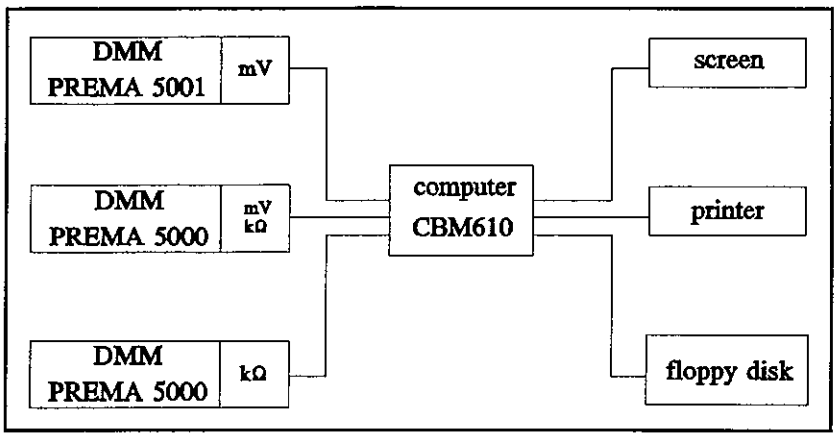

Fig. 4: Data acquisition system (schematic)
DMM = digital multimeter

channel	DMM 5001	DMM 5000	DMM 5000
0	/	T_A Pt-100 200 mV	R_{normal} 200 kΩ
1	**Pyrr. (MOH)** 200 mV	$T_{B,Pyrr}$ **(MOH)** 200 mV	/
2	**Pyrr. (AES)** 200 mV	**Pyran. (MOH)** 200 mV	$T_{B,Pyrr}$ **(AES)** 200 kΩ
3	**PIR (SMHI)** 200 mV	T_D **(SMHI)** 200 kΩ	T_B **(SMHI)** 200 kΩ
4	**PIR (NASA)** 200 mV	T_D **(NASA)** 200 kΩ	T_B **(NASA)** 200 kΩ
5	**PIR (AES)** 200 mV	/	T_B **(AES)** 200 kΩ
6	**PIR (MOH)** 200 mV	/	T_B **(MOH)** 200 kΩ
7	**Pyrg. (EKO)** 200 mV	/	T_B **(EKO)** 200 kΩ
8	**PIR-Foot (MRF)** 200 mV	/	T_B **(MRF)** 200 kΩ

Fig. 5: Channels of the data acquisition system
(with full scale given)

```
MOH LW-Sensor Intercomperison

date: 200789          time: 201218          readings:  120
+001.8  +128.7  +127.7  +124.9  +125.3  +123.3  +125.2  +000.0  +121.6  +000.0
+015.3  +015.2  +000.6  +015.2  +014.7  +074.1  +074.1  +000.0  +000.0  +000.0
+906.7  +000.0  +014.6  +015.2  +014.8  +016.7  +015.2  +000.0  +013.6  +000.0

date: 200789          time: 211218          readings:  120
+001.6  +109.3  +106.9  +103.8  +105.8  +101.7  +104.6  +000.0  +101.5  +000.0
+013.9  +013.9  -000.6  +013.9  +013.1  +074.1  +074.1  +000.0  +000.0  +000.0
+906.7  +000.0  +012.7  +014.0  +013.4  +015.5  +014.0  +000.0  +012.0  +000.0

date: 200789          time: 221218          readings:  120
+001.7  +108.1  +106.6  +102.9  +104.5  +100.6  +103.8  +000.0  +100.3  +000.0
+012.8  +012.7  -000.5  +012.7  +011.7  +074.1  +074.1  +000.0  +000.0  +000.0
+906.6  +000.0  +011.1  +012.8  +012.0  +014.3  +012.7  +000.0  +010.7  +000.0

date: 200789          time: 231219          readings:  120
+001.7  +107.1  +105.9  +101.8  +103.4  +099.5  +102.8  +000.0  +099.1  +000.0
+012.1  +011.9  -000.5  +012.0  +010.9  +074.1  +074.1  +000.0  +000.0  +000.0
+906.6  +000.0  +010.3  +012.0  +011.2  +013.6  +011.9  +000.0  +010.0  +000.0

date: 210789          time: 001218          readings:  120
+001.8  +106.2  +105.1  +101.8  +102.5  +098.7  +102.0  +000.0  +098.3  +000.0
+011.1  +011.1  -000.5  +011.2  +010.0  +074.1  +074.1  +000.0  +000.0  +000.0
+906.6  +000.0  +009.3  +011.3  +010.3  +012.8  +011.2  +000.0  +009.1  +000.0

date: 210789          time: 011219          readings:  120
+001.8  +110.0  +109.9  +105.7  +106.7  +103.5  +106.6  +000.0  +102.6  +000.0
+010.7  +010.6  -000.4  +010.7  +009.5  +074.1  +074.1  +000.0  +000.0  +000.0
+906.6  +000.0  +008.9  +010.8  +009.8  +012.2  +010.6  +000.0  +008.6  +000.0

date: 210789          time: 021218          readings:  120
+001.8  +125.0  +126.0  +123.0  +122.8  +121.6  +123.4  +000.0  +119.0  +000.0
+010.7  +010.5  -000.1  +010.8  +009.8  +074.1  +074.1  +000.0  +000.0  +000.0
+906.6  +000.0  +009.3  +010.8  +009.9  +012.2  +010.7  +000.0  +008.8  +000.0

date: 210789          time: 031218          readings:  120
+001.8  +129.6  +130.5  +127.9  +127.4  +126.8  +128.2  +000.0  +123.7  +000.0
+011.2  +011.0  -000.0  +011.3  +010.4  +074.1  +074.1  +000.0  +000.0  +000.0
+906.7  +000.0  +010.3  +011.2  +010.5  +012.6  +011.1  +000.0  +009.4  +000.0

date: 210789          time: 041218          readings:  120
+001.8  +129.7  +130.3  +127.8  +127.5  +126.7  +128.0  +000.0  +123.7  +000.0
+011.5  +011.4  +002.5  +011.6  +010.8  +074.1  +074.1  +000.0  +000.0  +000.0
+906.7  +000.0  +010.8  +011.6  +010.9  +013.0  +011.5  +000.0  +009.7  +000.0

date: 210789          time: 051218          readings:  120
+001.8  +129.3  +130.3  +128.1  +127.7  +126.5  +128.0  +000.0  +123.9  +000.0
+011.9  +011.7  +011.9  +012.0  +011.3  +074.1  +074.1  +000.0  +000.0  +000.0
+906.6  +000.0  +011.2  +011.9  +011.3  +013.3  +011.8  +000.0  +010.2  +000.0

date: 210789          time: 061218          readings:  120
+001.7  +129.6  +130.6  +129.2  +128.9  +127.1  +128.7  +000.0  +124.9  +000.0
+012.6  +012.5  +022.5  +012.7  +012.1  +074.1  +074.1  +000.0  +000.0  +000.0
+906.7  +000.0  +012.1  +012.6  +012.1  +014.0  +012.5  +000.0  +010.9  +000.0
```

Fig. 6: Facsimile of an original hourly data printout
(for channel identification, see Fig. 5)

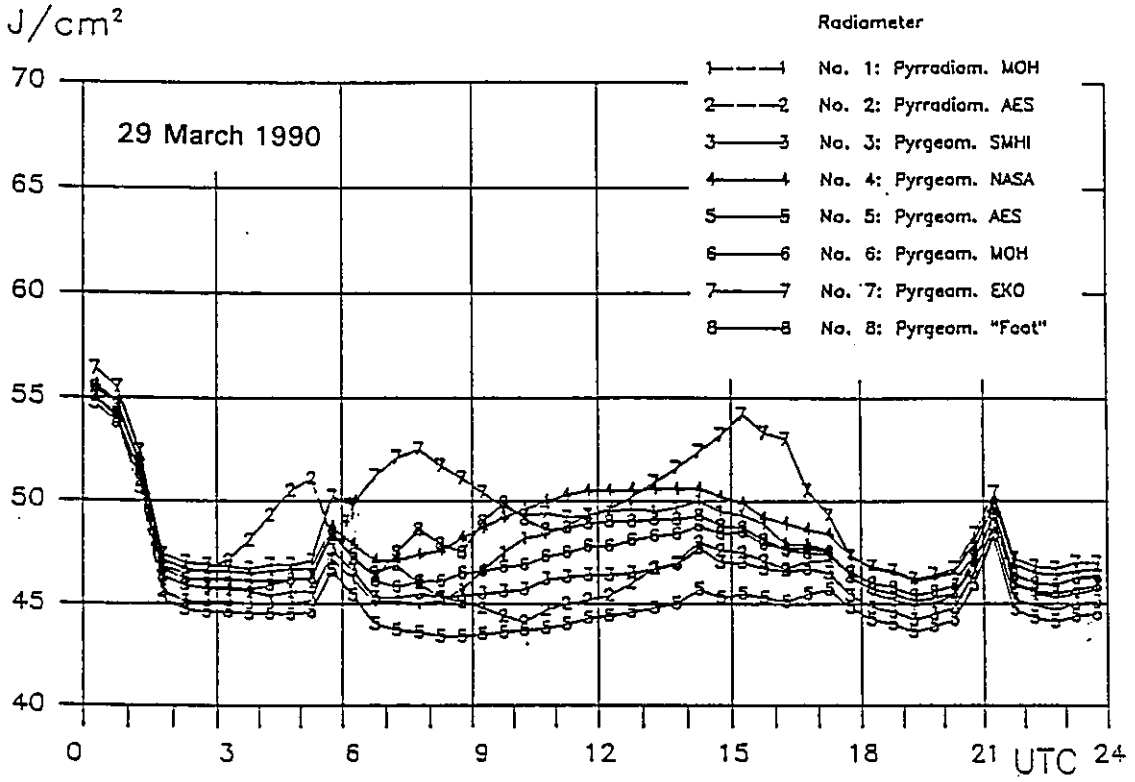

Fig. 7: Diurnal cycle of halfhourly sums of atmospheric radiation A, measured with eight different instruments on 29 March 1990

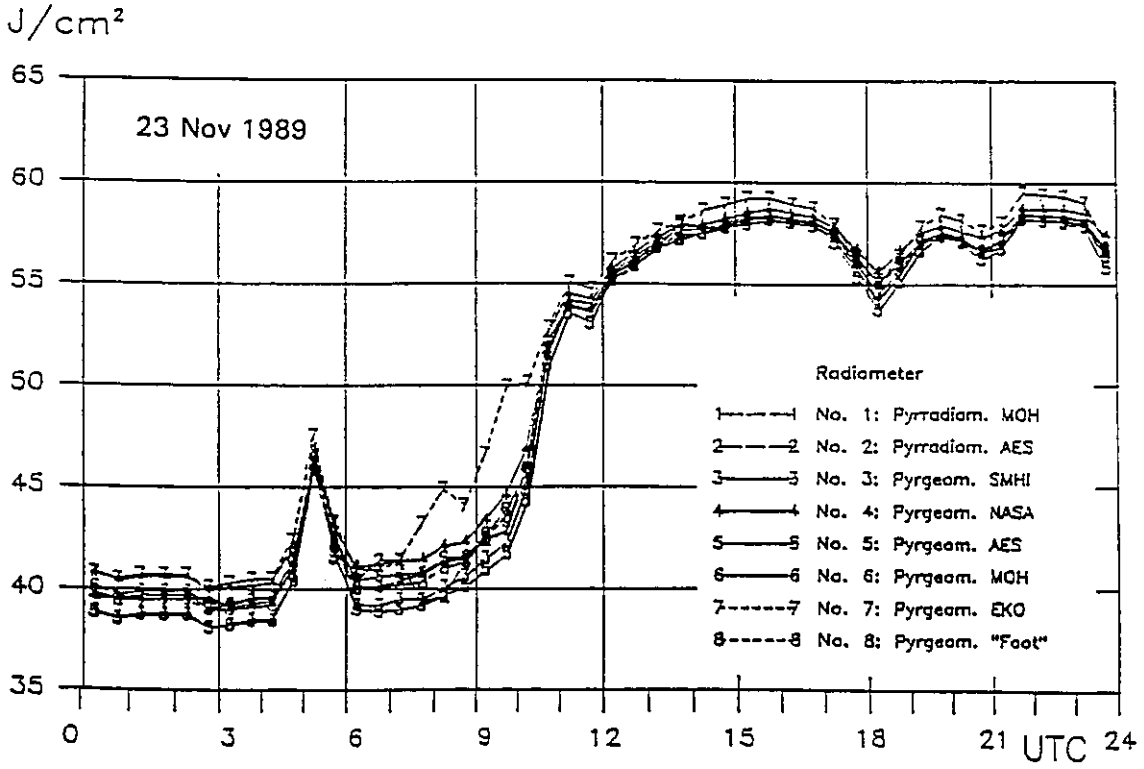

Fig. 8: Same as Fig. 7 but on 23 November 1989

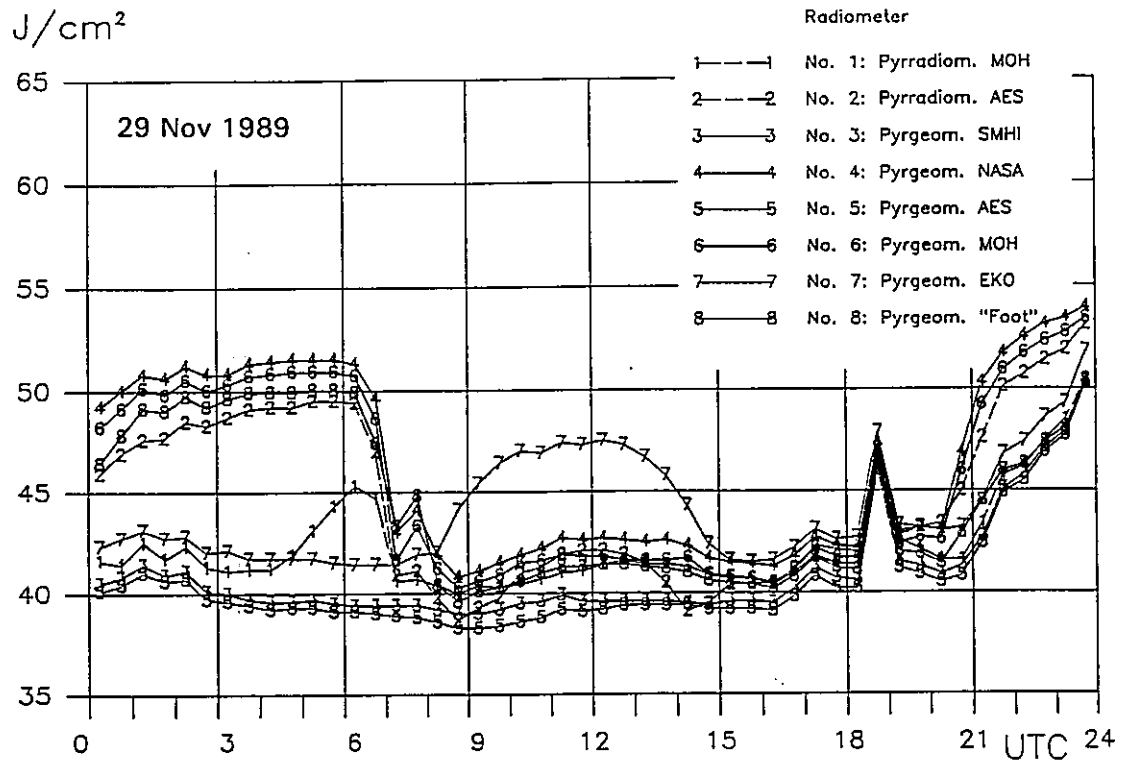

Fig. 9: Same as Fig. 7 but on 29 November 1989

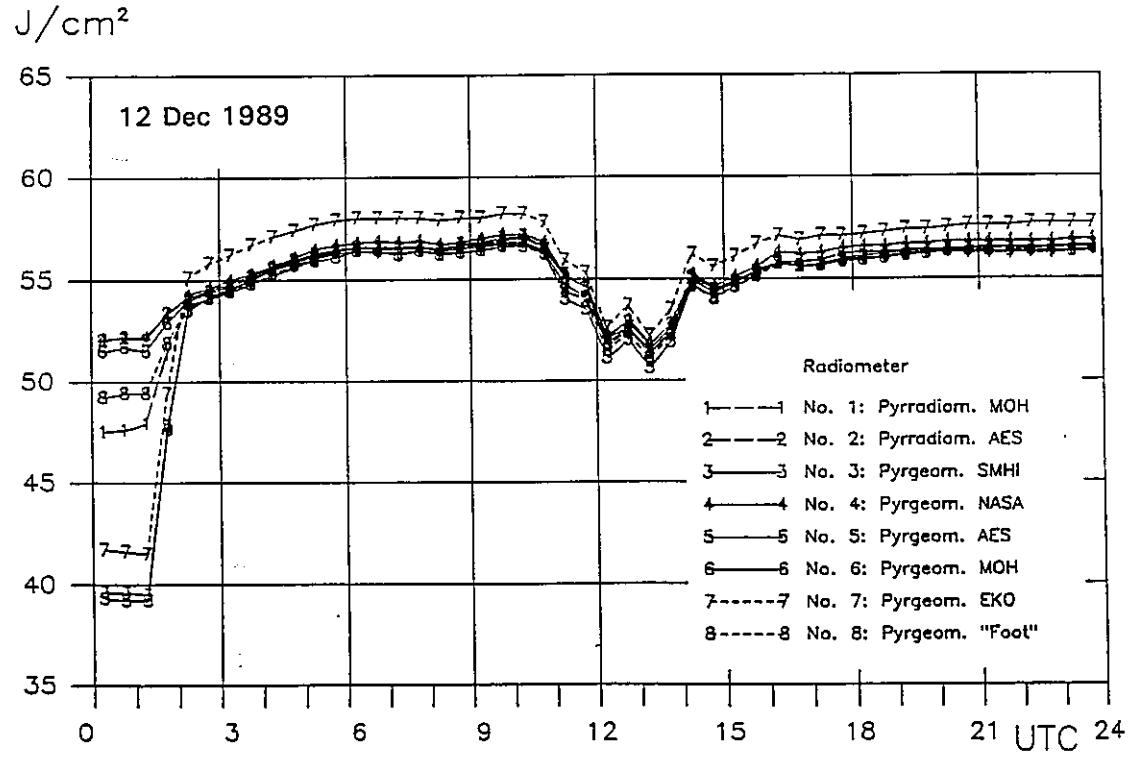

Fig. 10: Same as Fig. 7 but on 12 December 1989

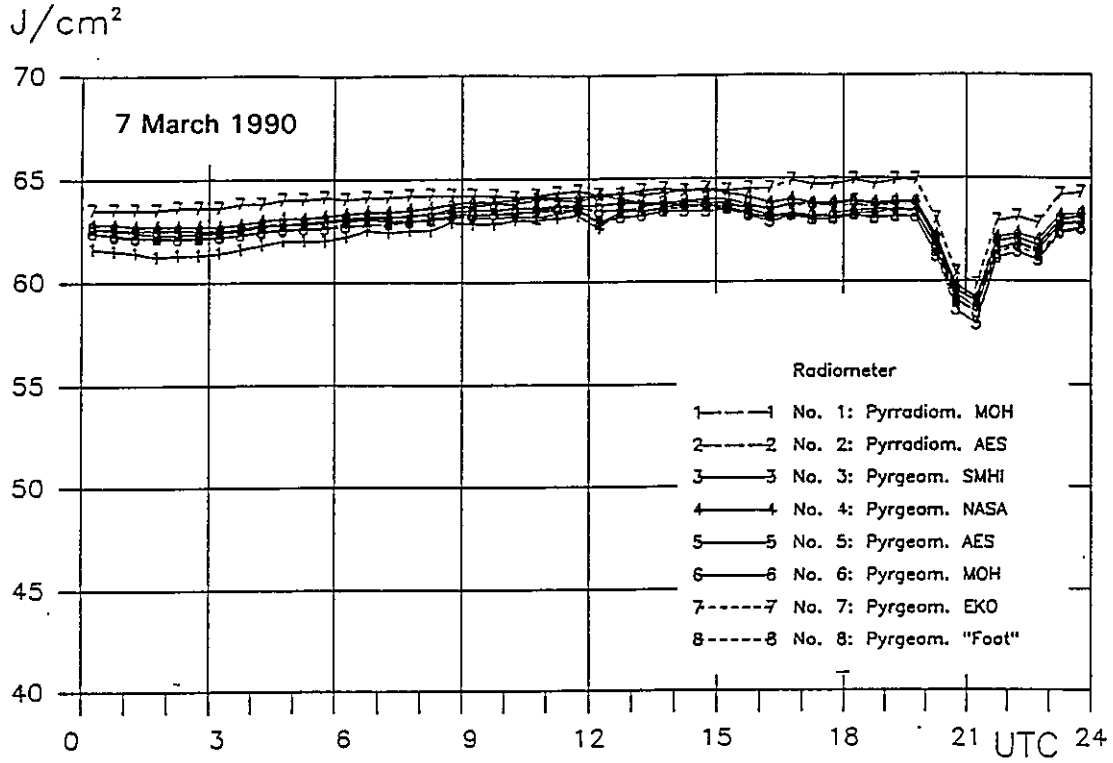

Fig. 11: Same as Fig. 7 but on 07 March 1990

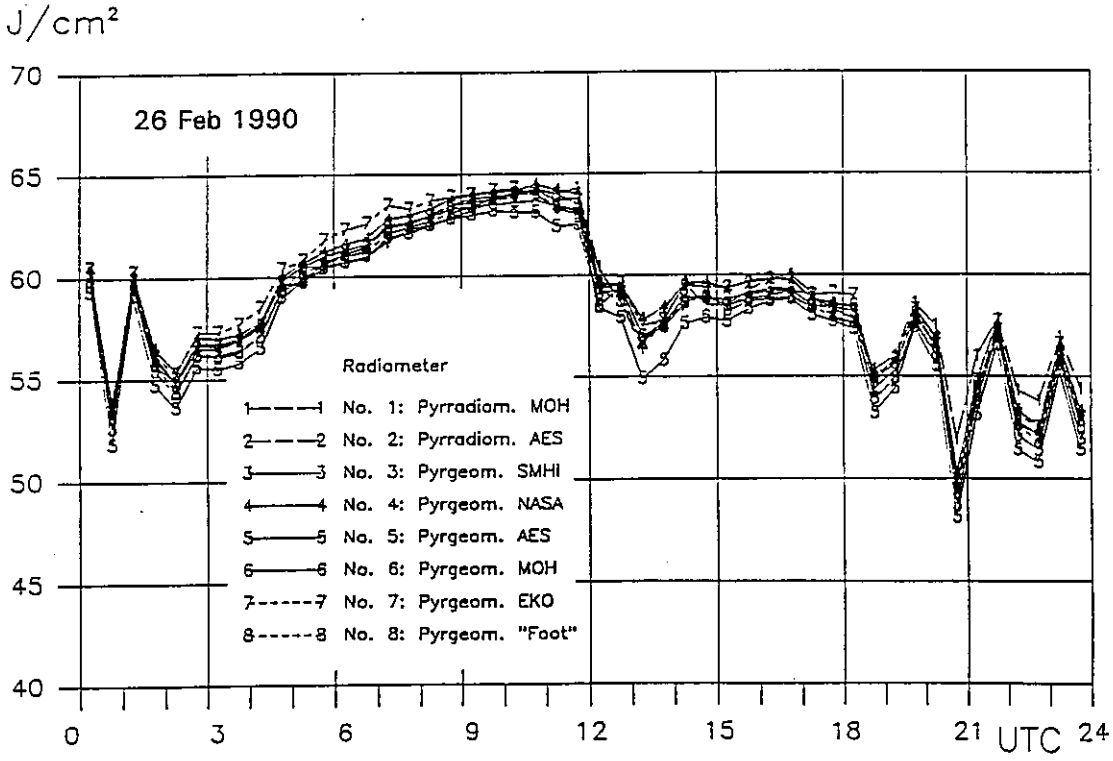

Fig. 12: Same as Fig. 7 but on 26 February 1990

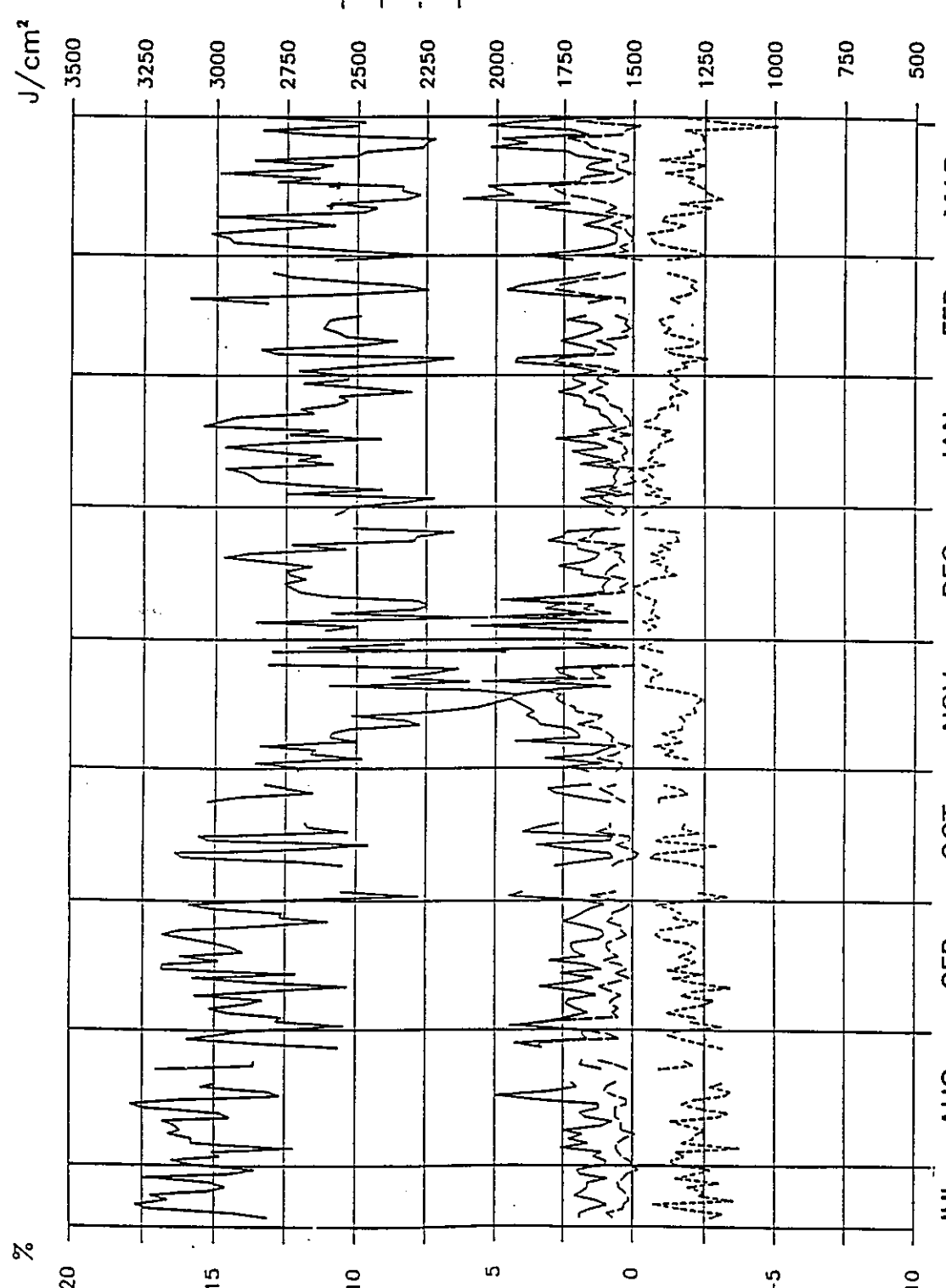

Fig. 13: Seasonal variation of daily sums of atmospheric radiation A, measured with four different instruments in 1989/90

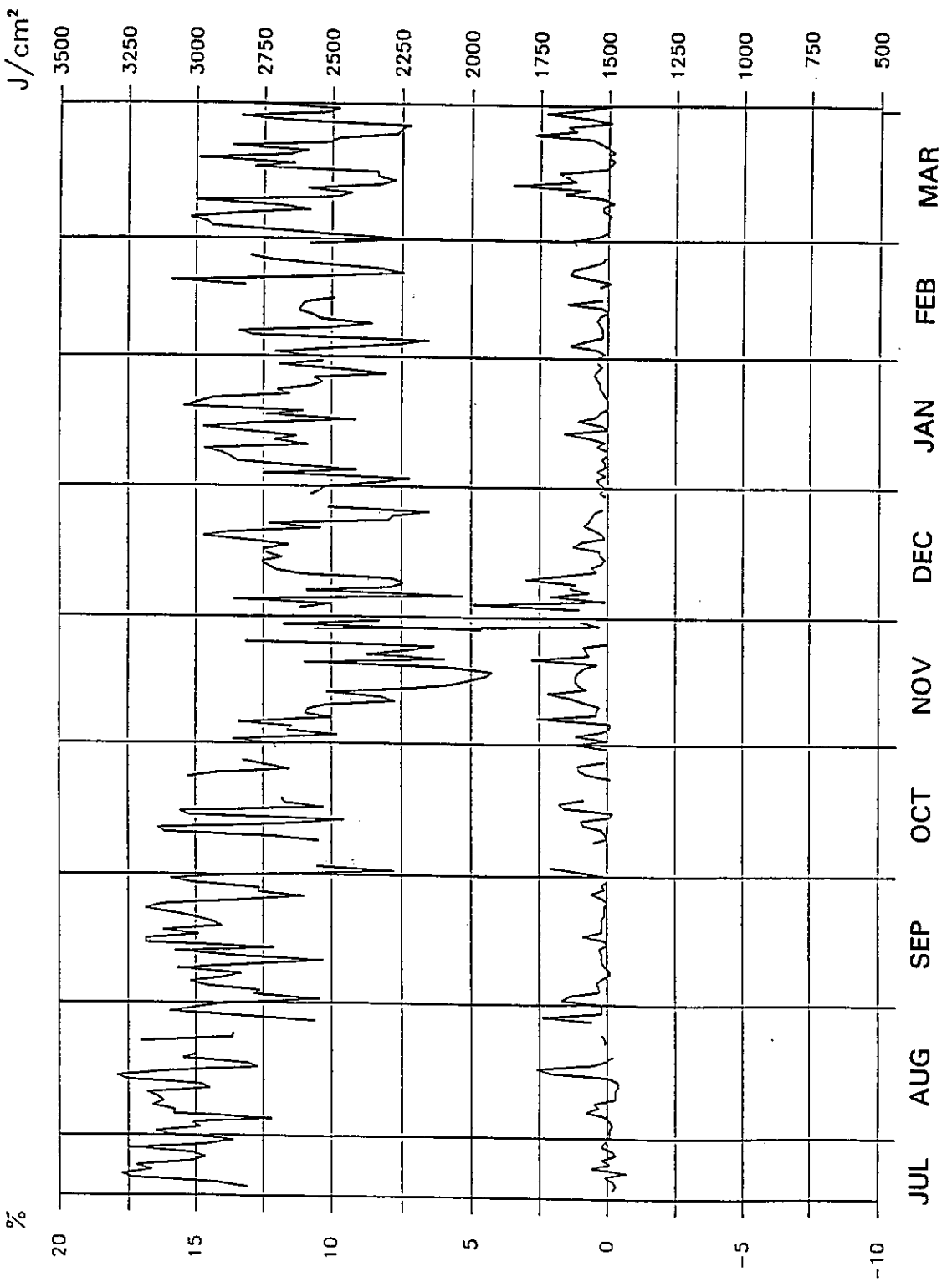

Fig. 14: Same as Fig. 13 but with different correction factors for the NASA pyrgeometer

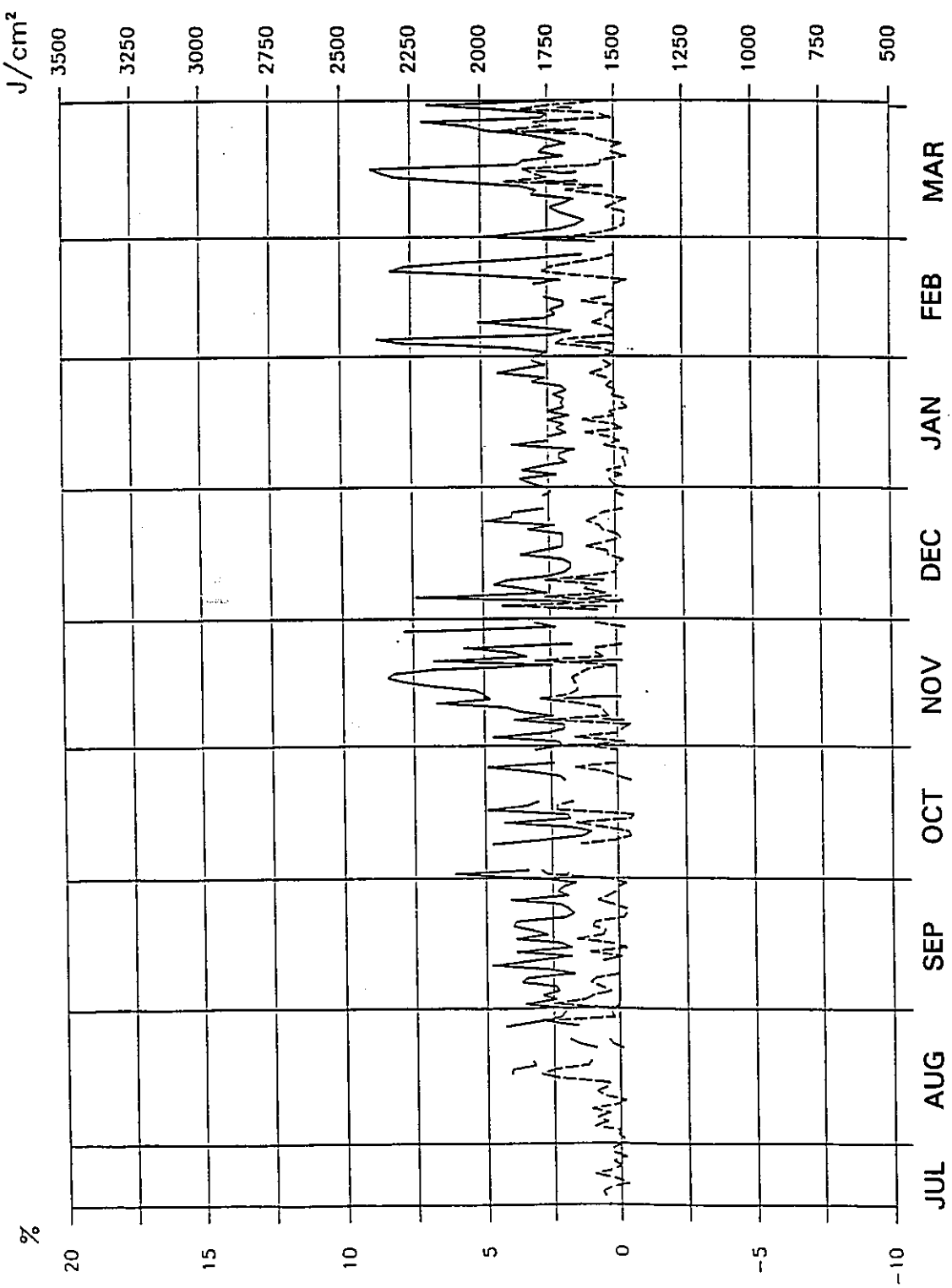

Fig. 15: Same as Fig. 13 but for two other pyrgeometers

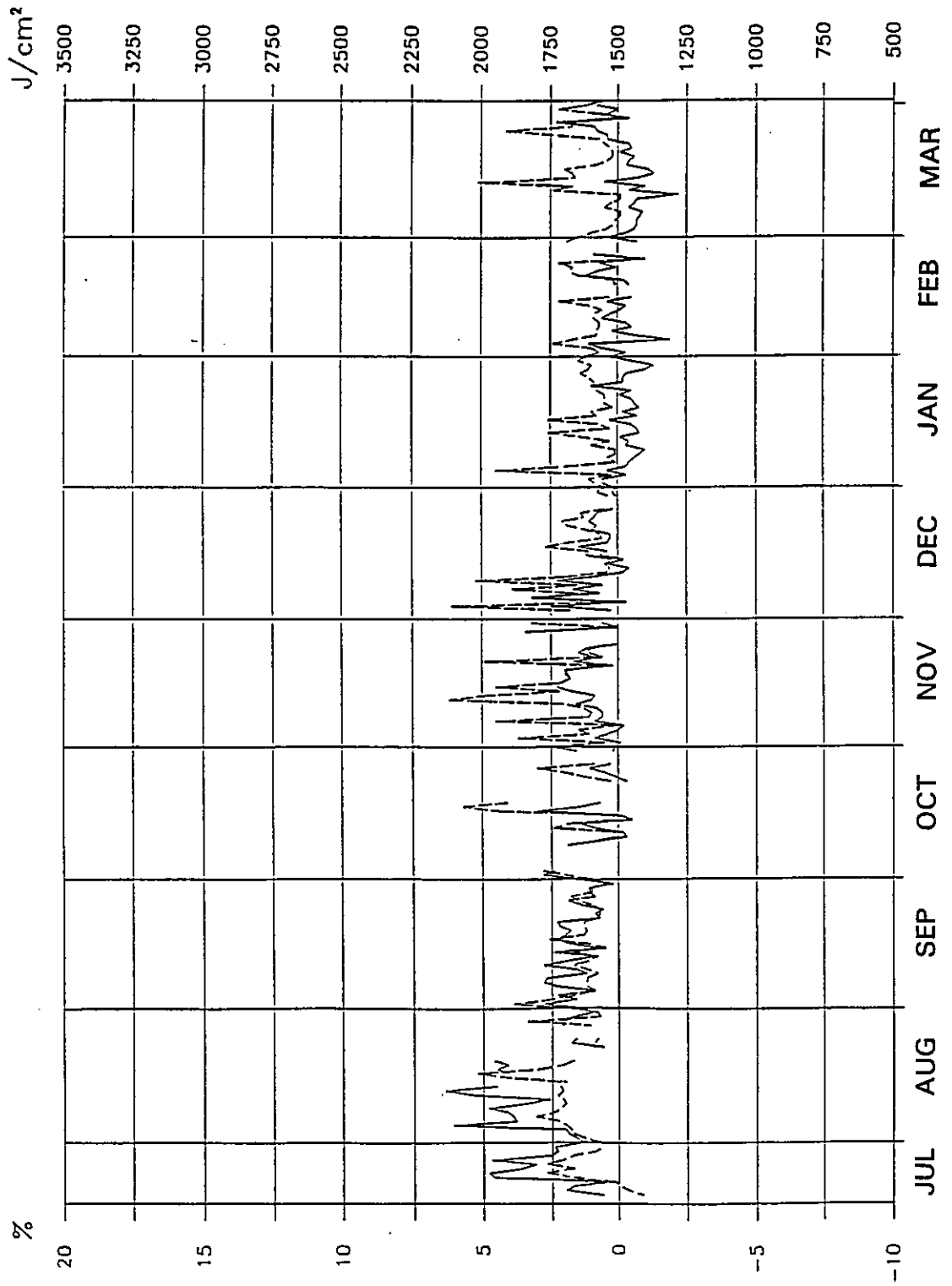

Fig. 16: Same as Fig. 13 but for two pyrradiometers

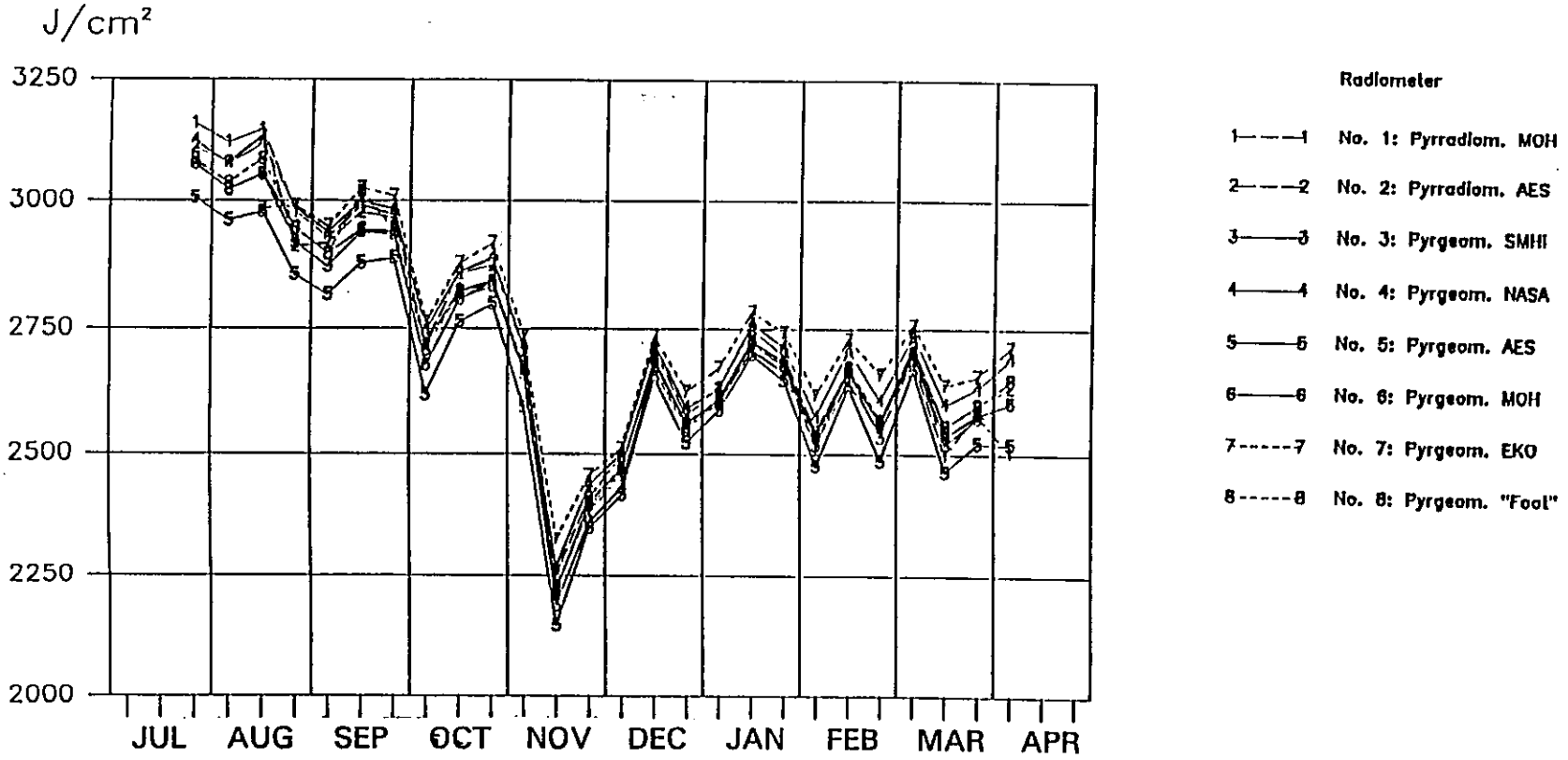

Fig. 17: Seasonal variation of ten-day means of daily sums of atmospheric radiation A, measured with eight different instruments in 1989/90

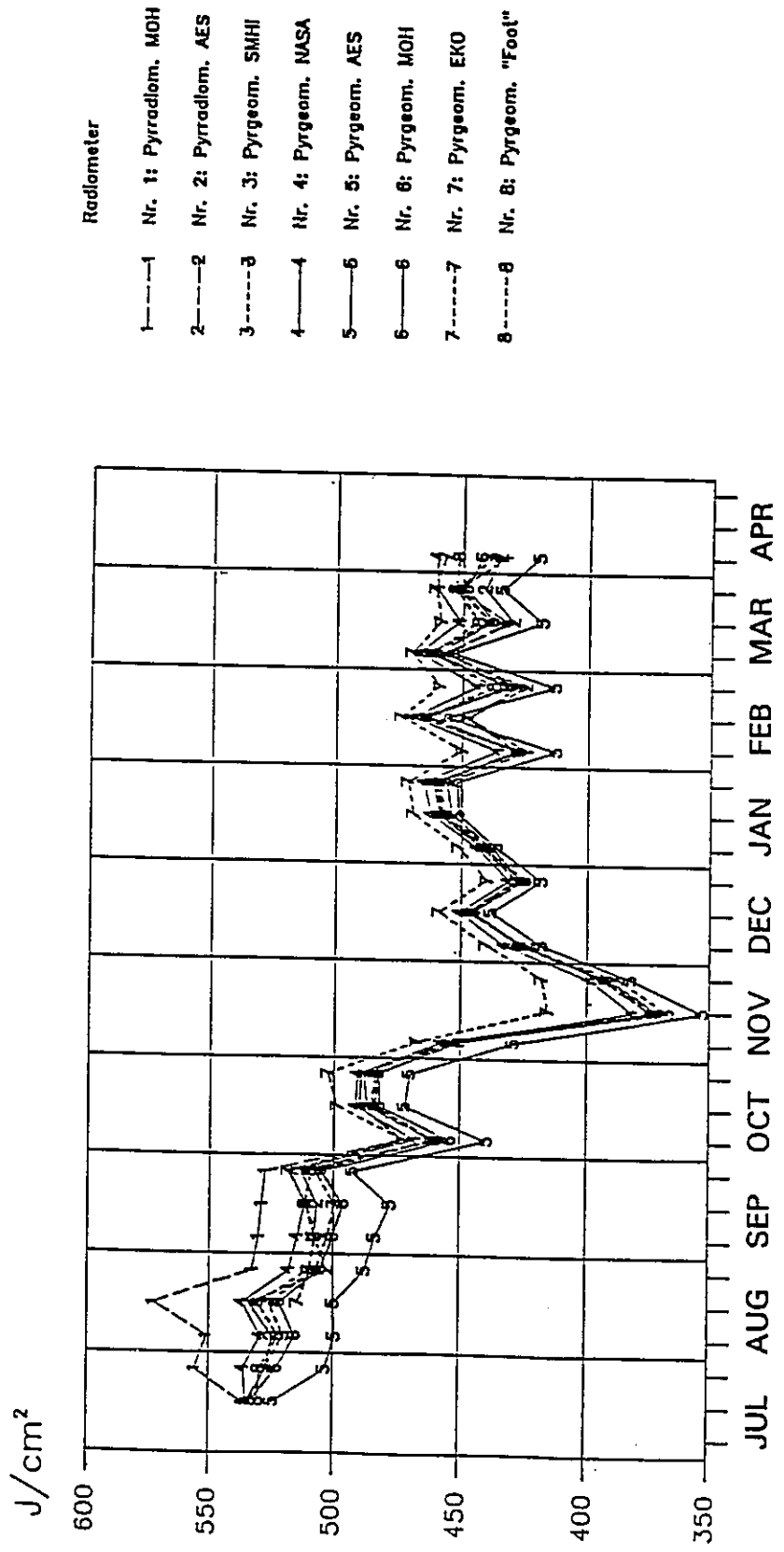

Fig. 18: Seasonal variation of ten-day means of the A-sums from 0930 to 1330 UTC, measured with eight different instruments in 1989/90

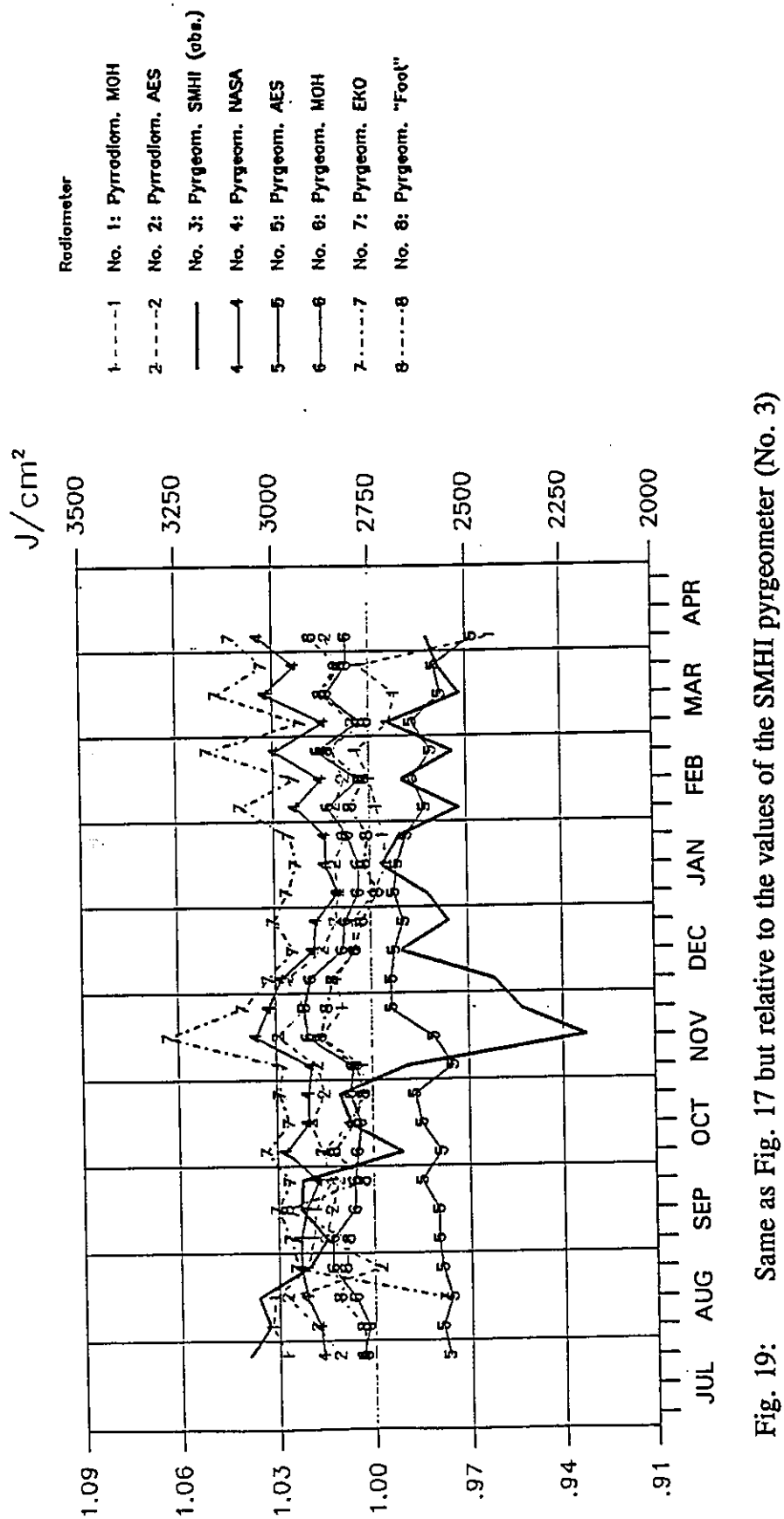

Fig. 19: Same as Fig. 17 but relative to the values of the SMHI pyrgeometer (No. 3)

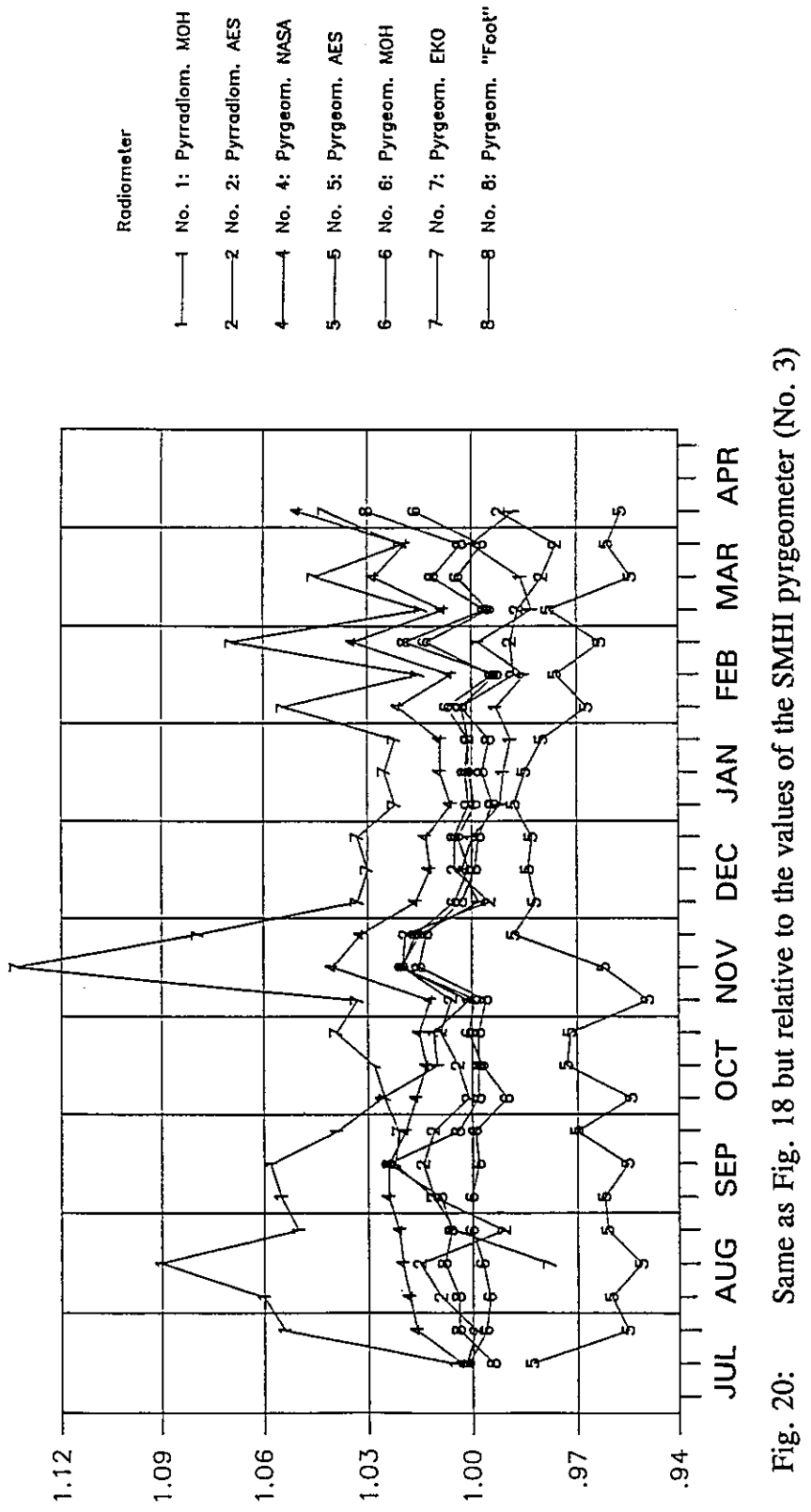

Fig. 20: Same as Fig. 18 but relative to the values of the SMHI pyrgeometer (No. 3)

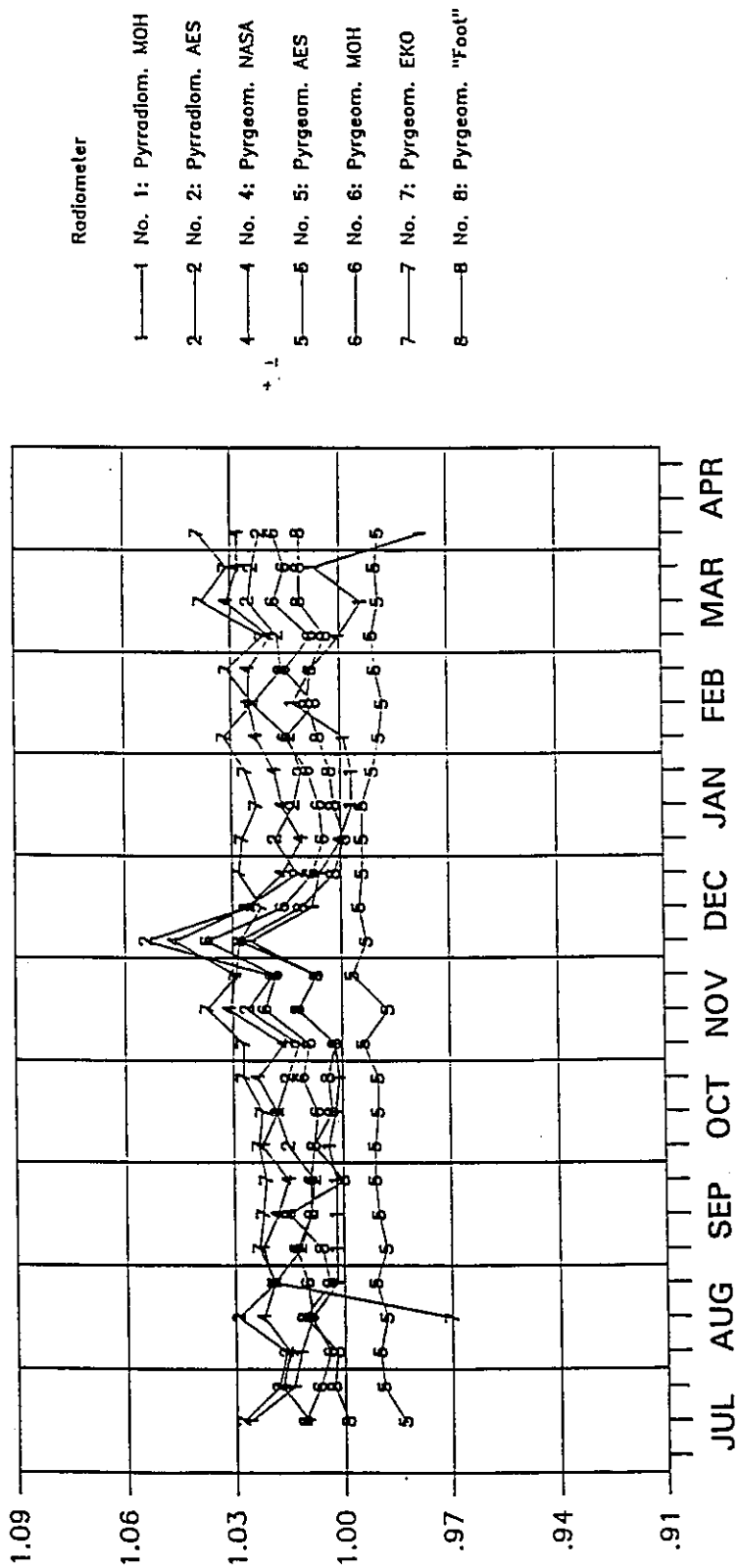

Fig. 21: Seasonal variation of ten-day means of the A-sums from 1800 to 2400 UTC, normalized to the values of the SMHI pyrgeometer

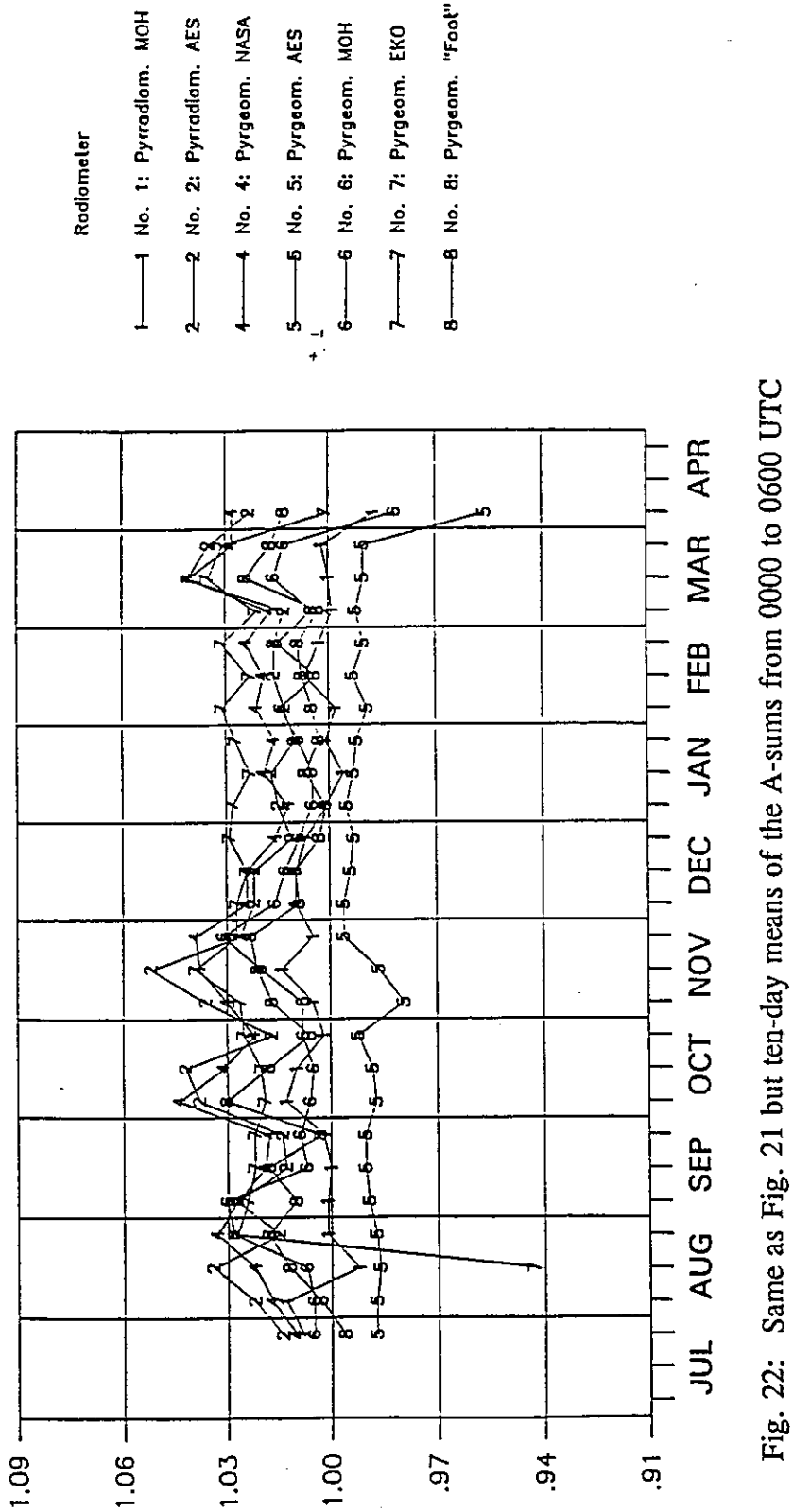

Fig. 22: Same as Fig. 21 but ten-day means of the A-sums from 0000 to 0600 UTC

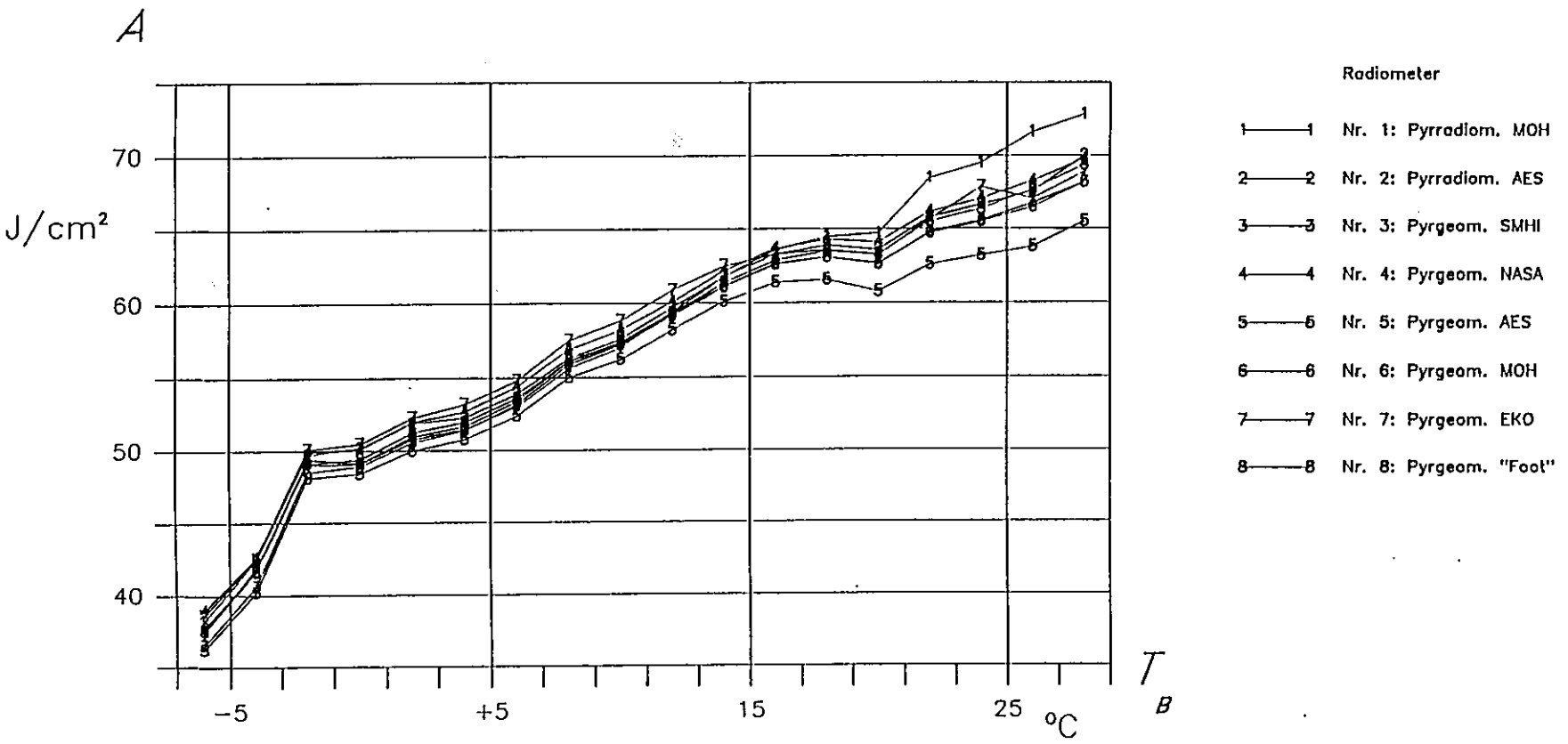

Fig. 23: Measured atmospheric radiation A versus body temperature T_B.
Means of halfhourly sums of A for given T_B-classes of 2 K width

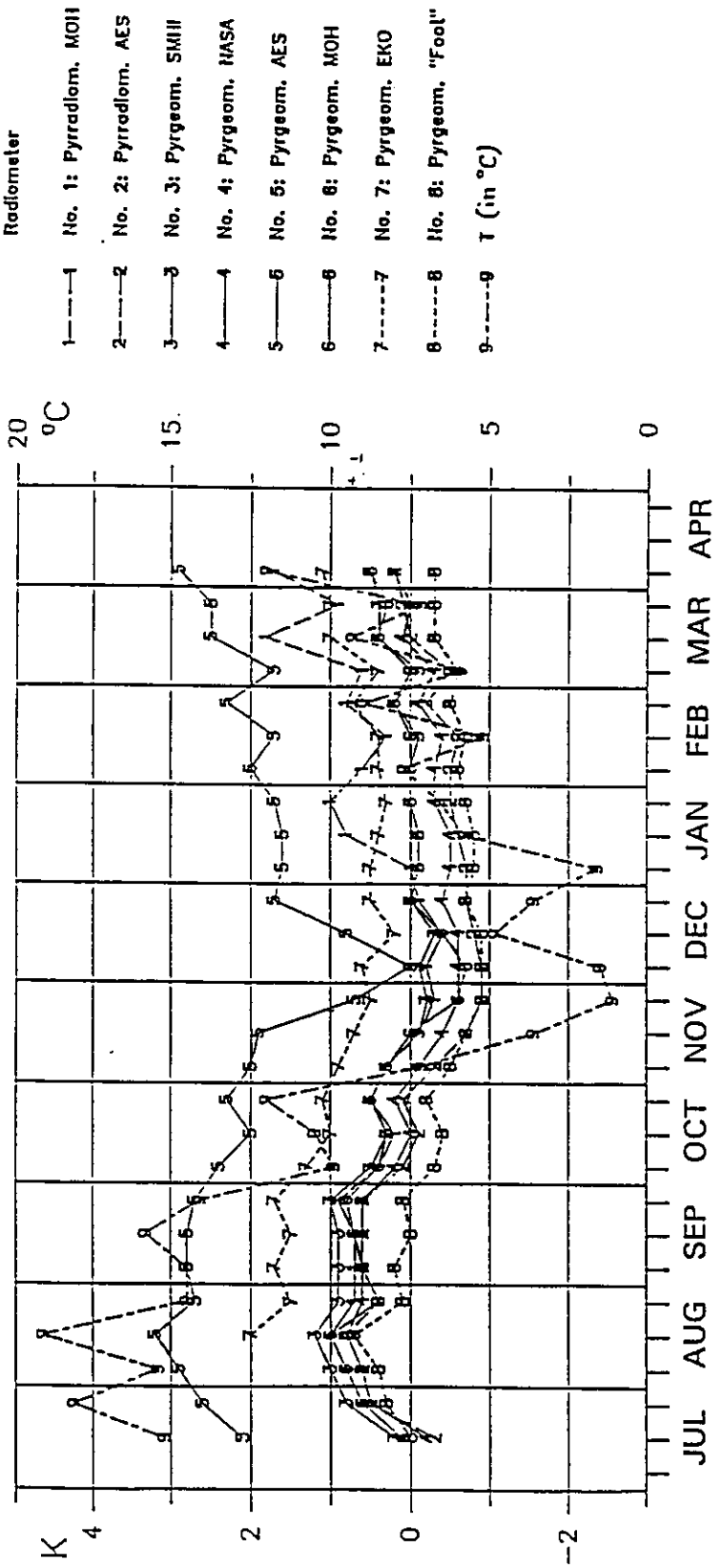

Fig. 26: Seasonal variation of the difference between body temperature T_B and air temperature T_A. Ten-day means

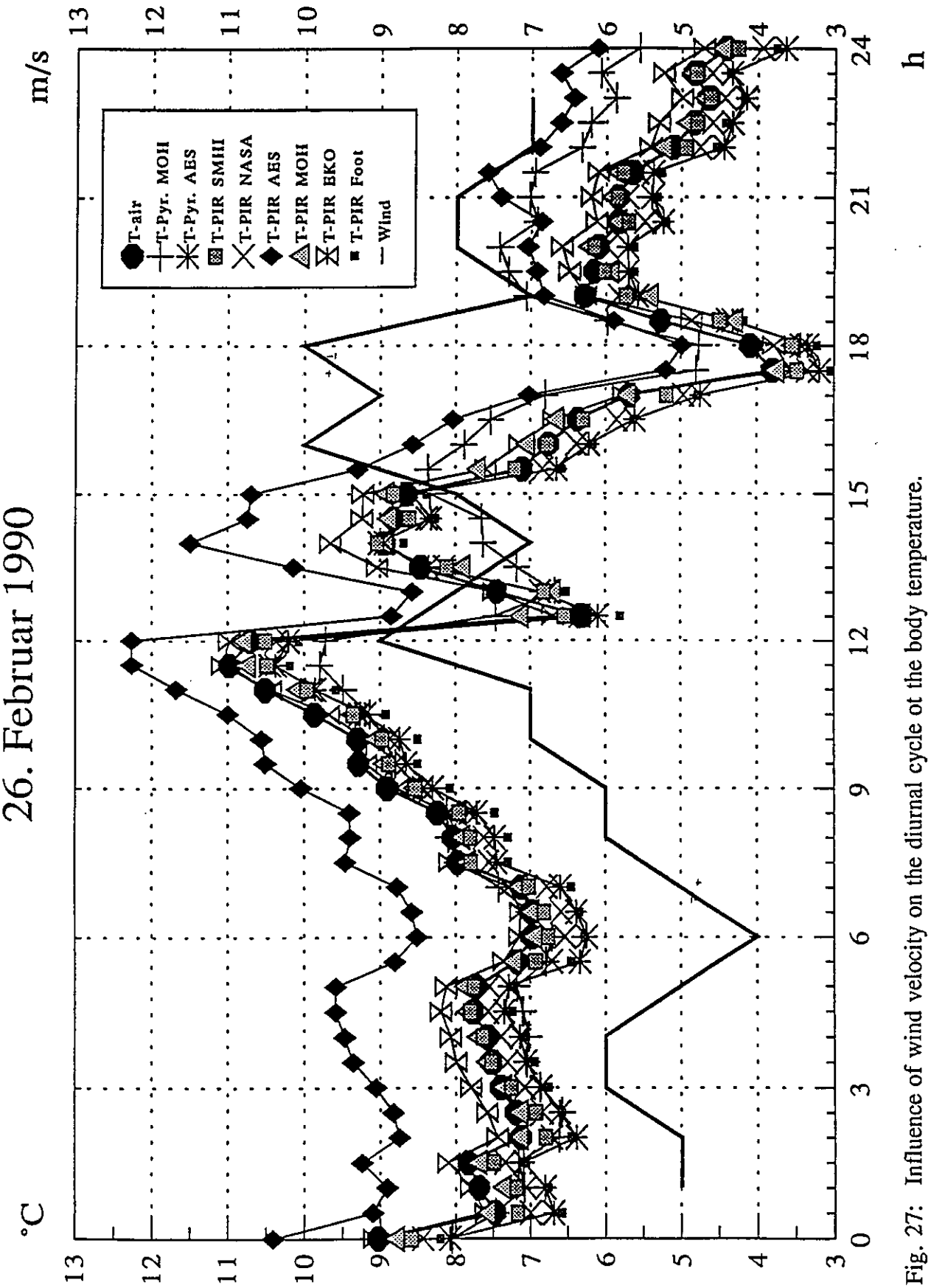

Fig. 27: Influence of wind velocity on the diurnal cycle ot the body temperature. Halfhourly means, 26 February 1990

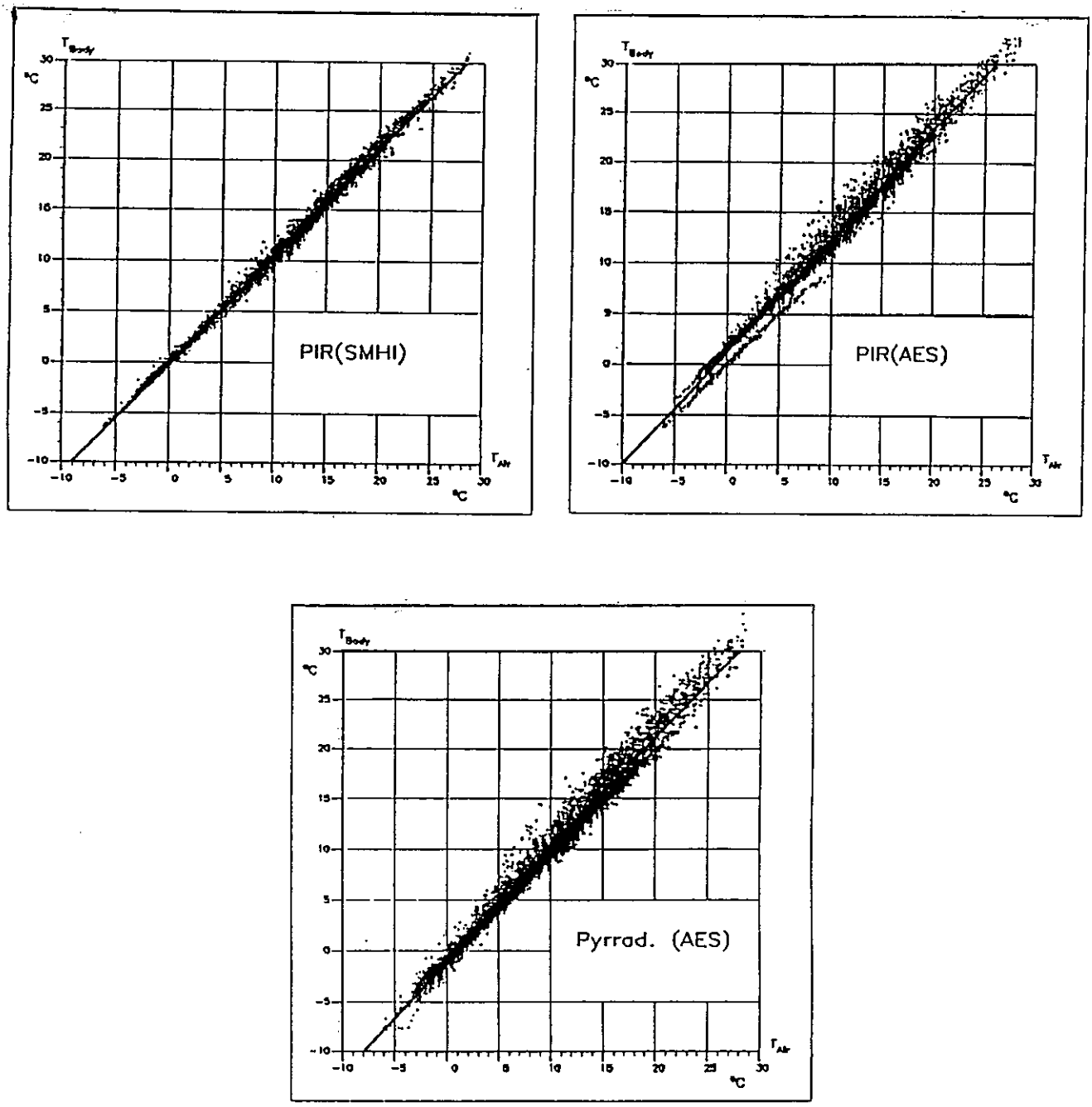

Fig. 28: Correlation of body temperature T_B and air temperature T_A. Halfhourly means

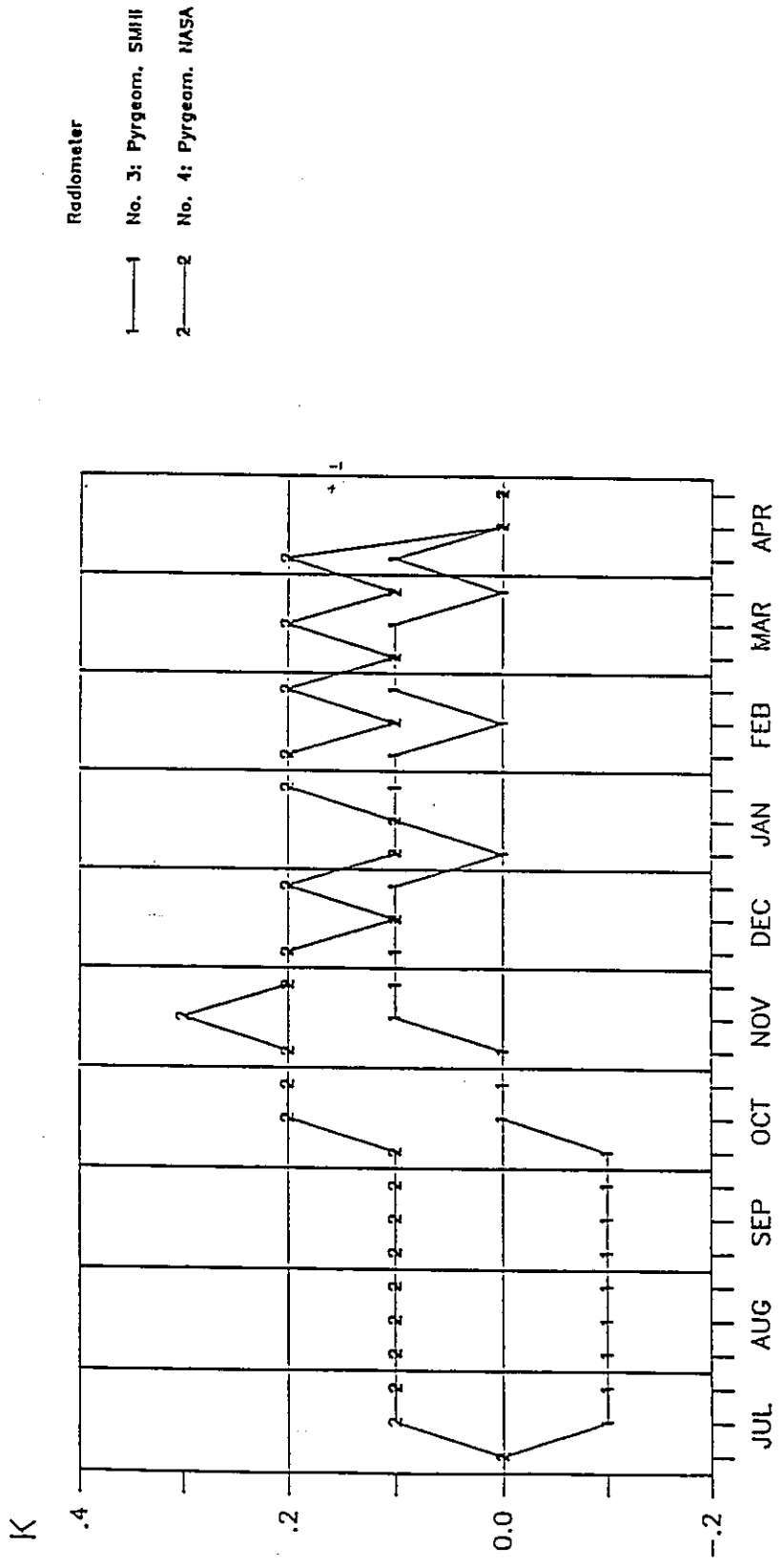

Fig. 29: Seasonal variation of the difference between body temperature T_B and dome temperature T_D. Ten-day means

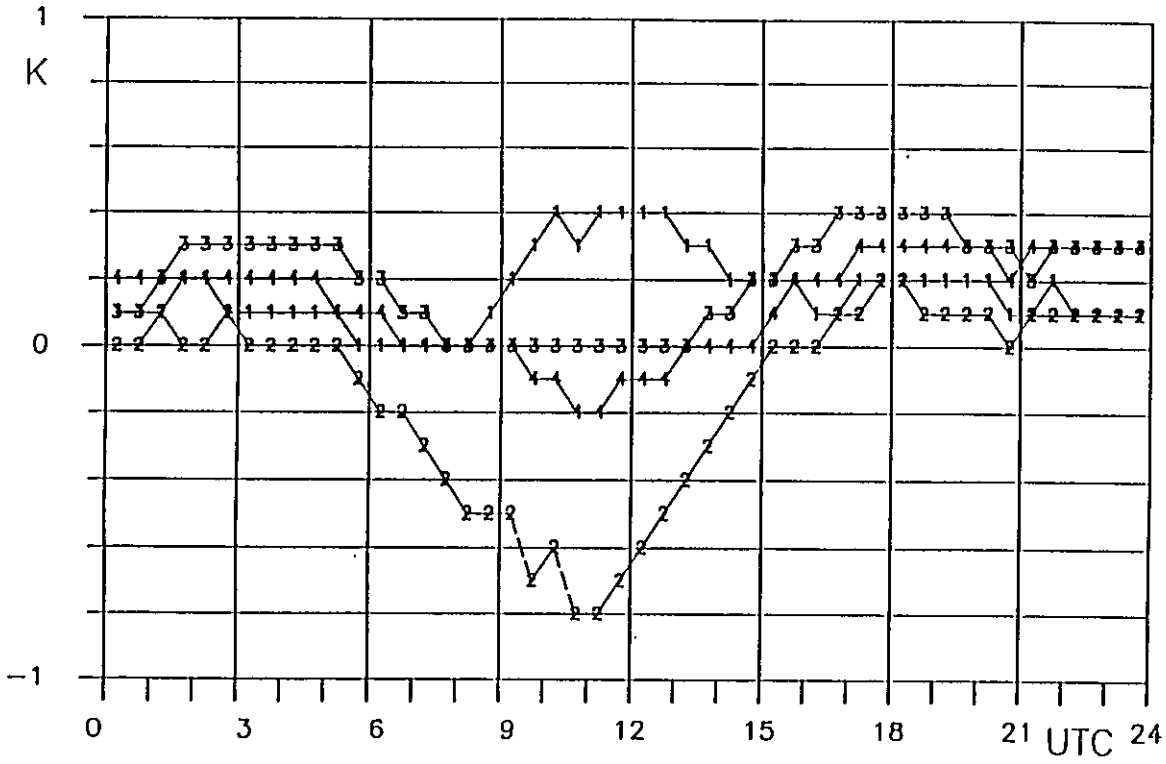

1———1 PIR_{SUN} 29.3.90 (sun with shadow-disc)

2———2 " 19.8.89 (sun without sh.-d.)

3———3 PIR_{NASA} 29.3.90 (sun with sh.-d.)

4———4 " 19.8.89 (sun without sh.-d.)

Fig. 30: Diurnal cycle of the difference between body temperature T_B and dome temperature T_D on two selected days

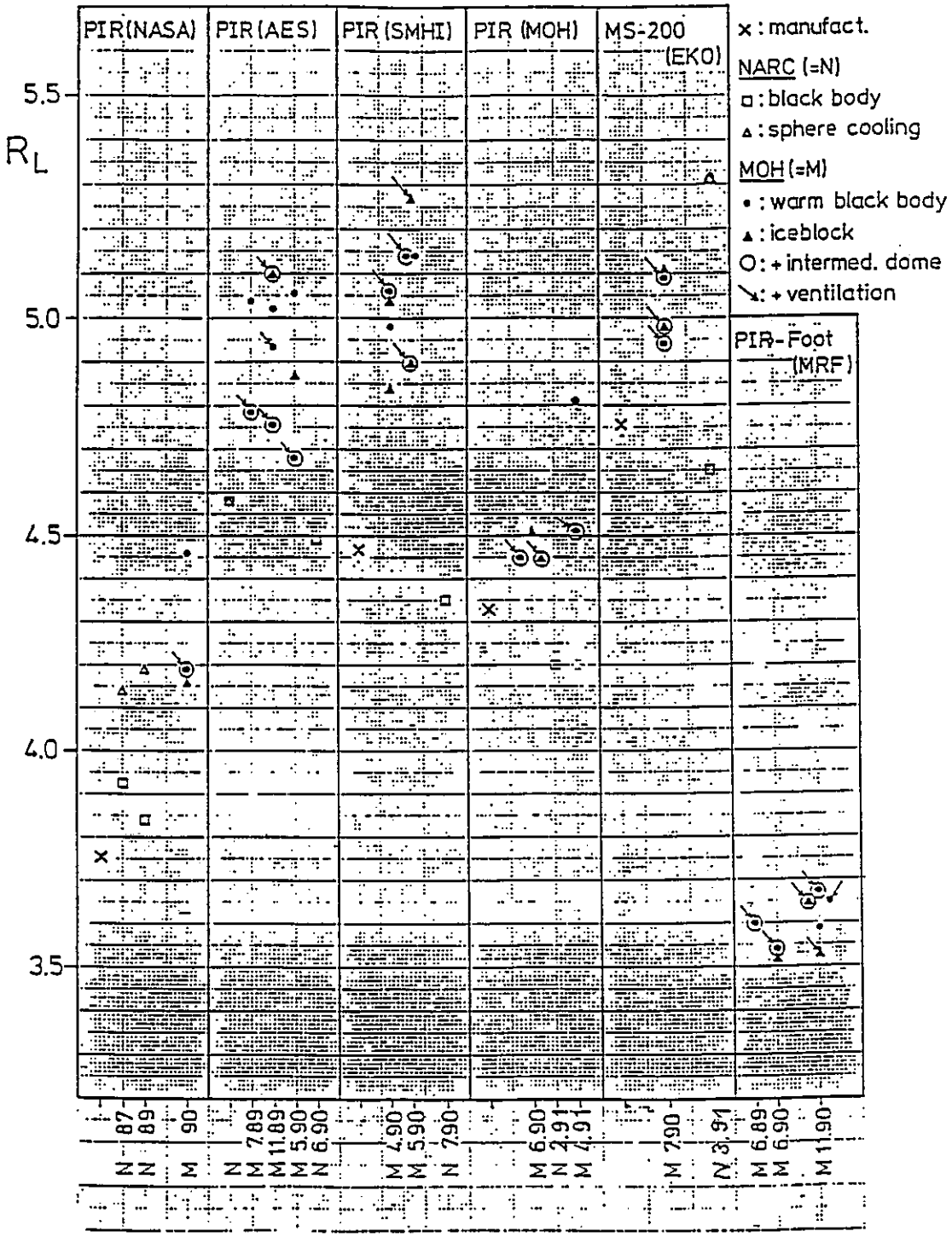

Fig. 31: Longwave responsivity R_L in $\mu V/W \cdot m^{-2}$ of six pyrgeometers after calibration by various laboratories in the years 1987-1990

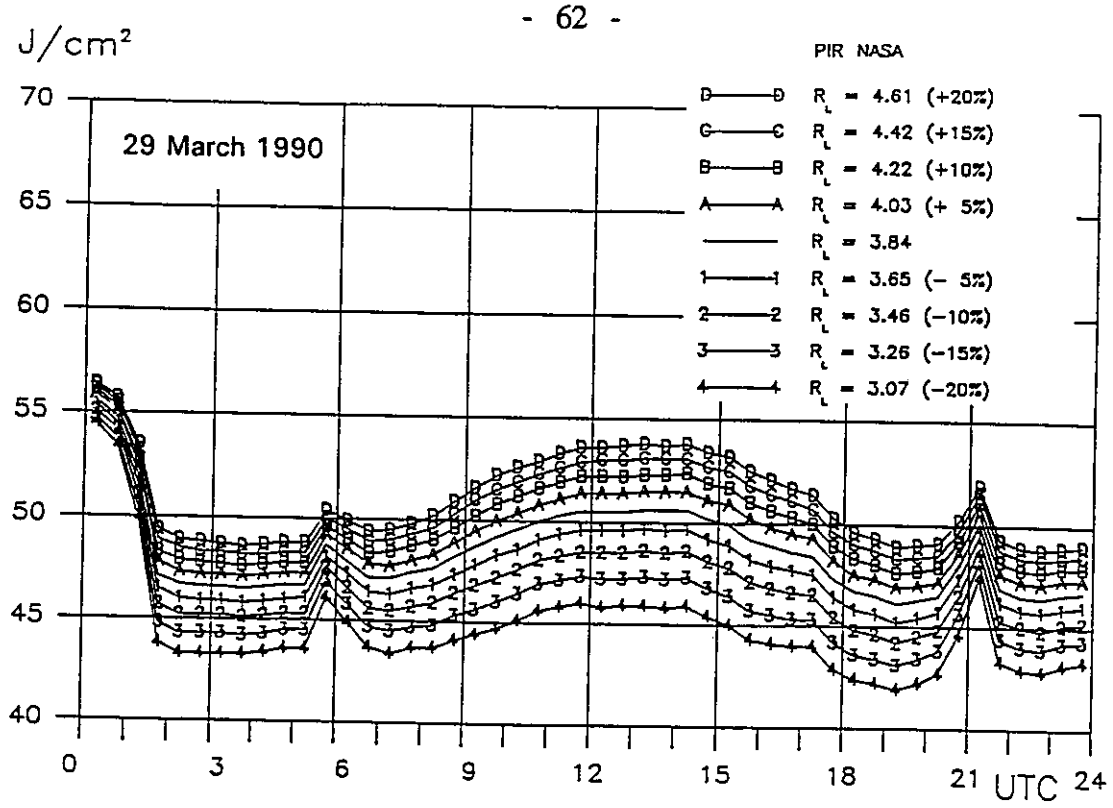

Fig. 32: Influence of the longwave responsivity R_L on the diurnal cycle of A, 29 March 1990. NASA pyrgeometer

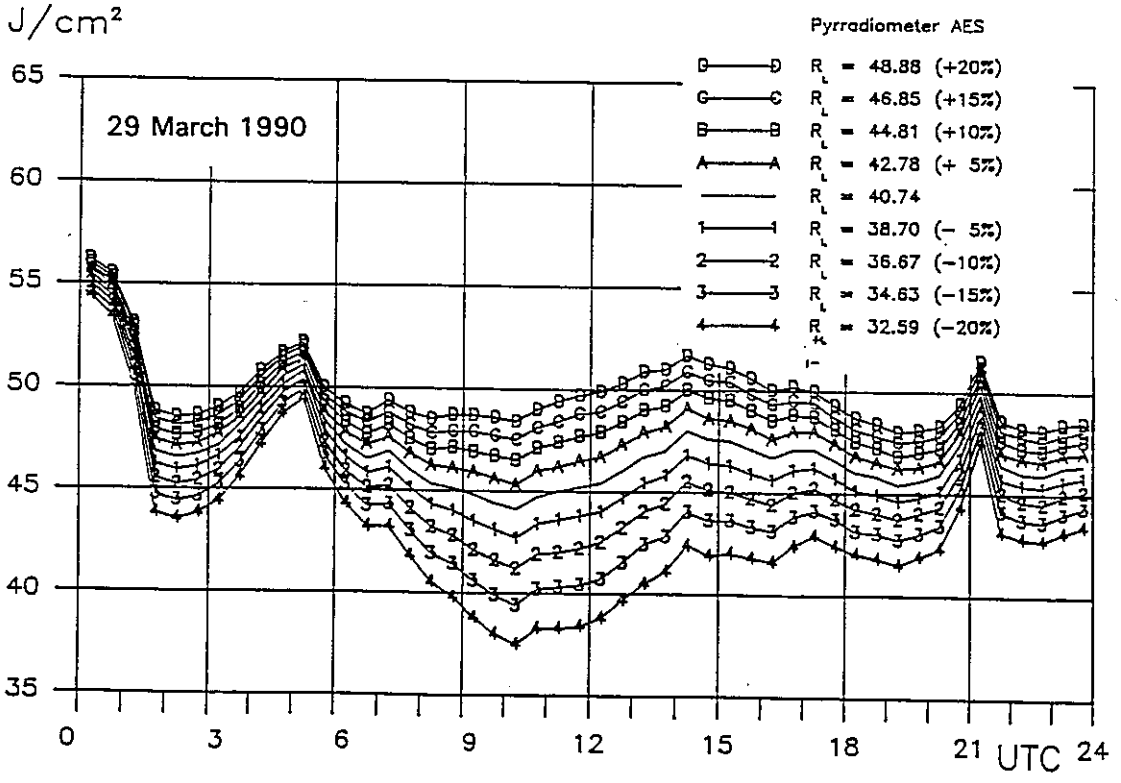

Fig. 33: Influence of the longwave responsivity R_L on the diurnal cycle of A, 29 March 1990. AES pyrgeometer

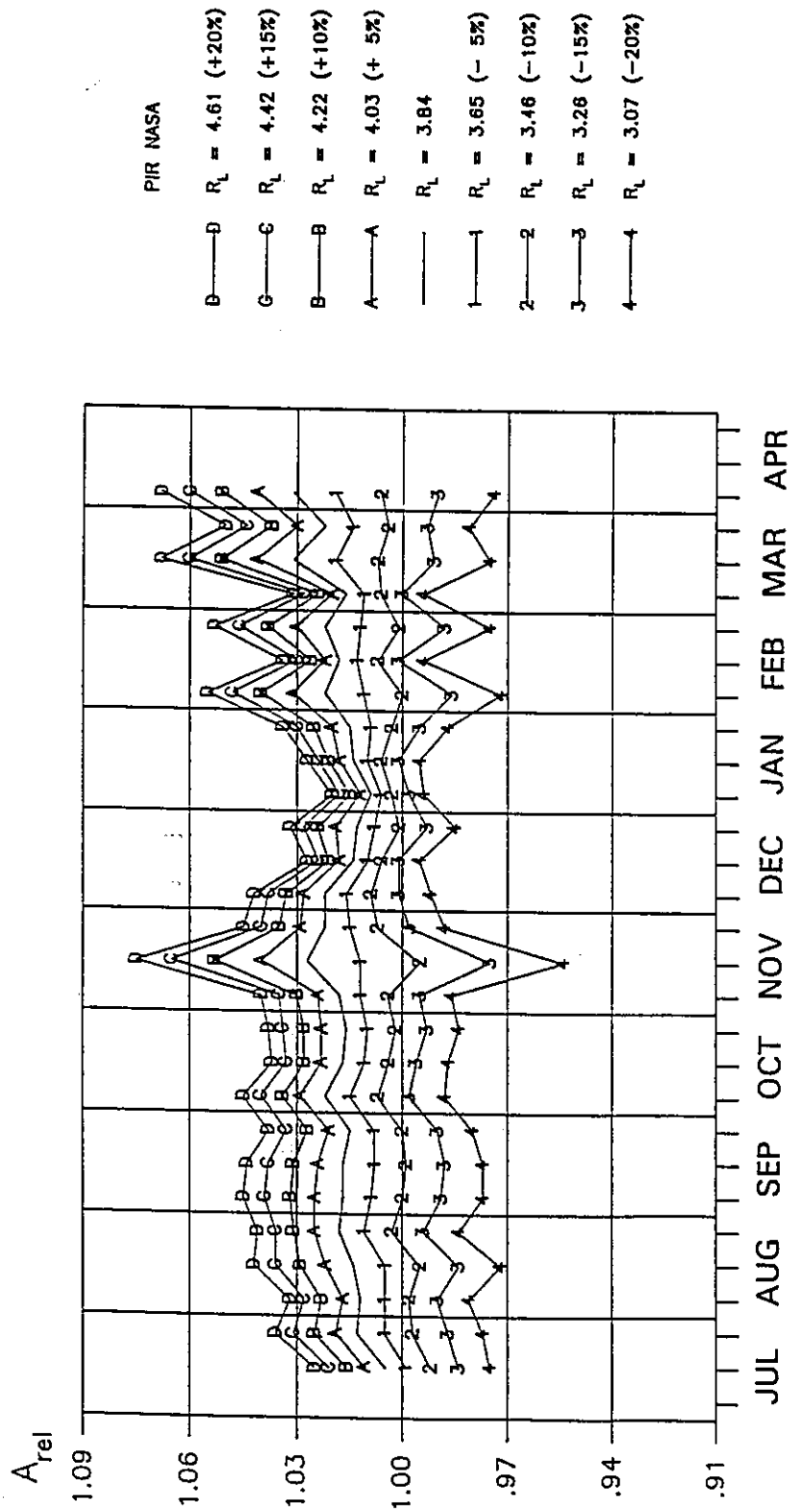

Fig. 34: Influence of the longwave responsivity R_L on the seasonal variation of A, 1989/90. NASA pyrgeometer

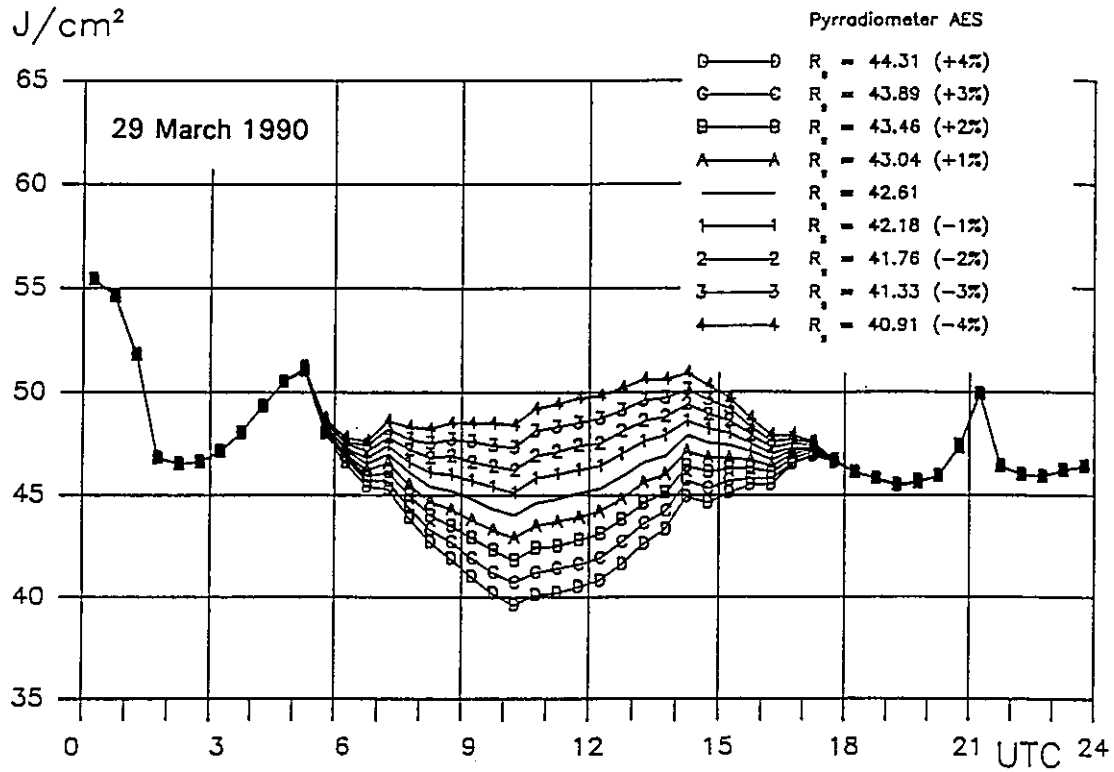

Fig. 35: Influence of the shortwave responsivity R_S on the diurnal cycle of A, 29 March 1990. AES pyrradiometer

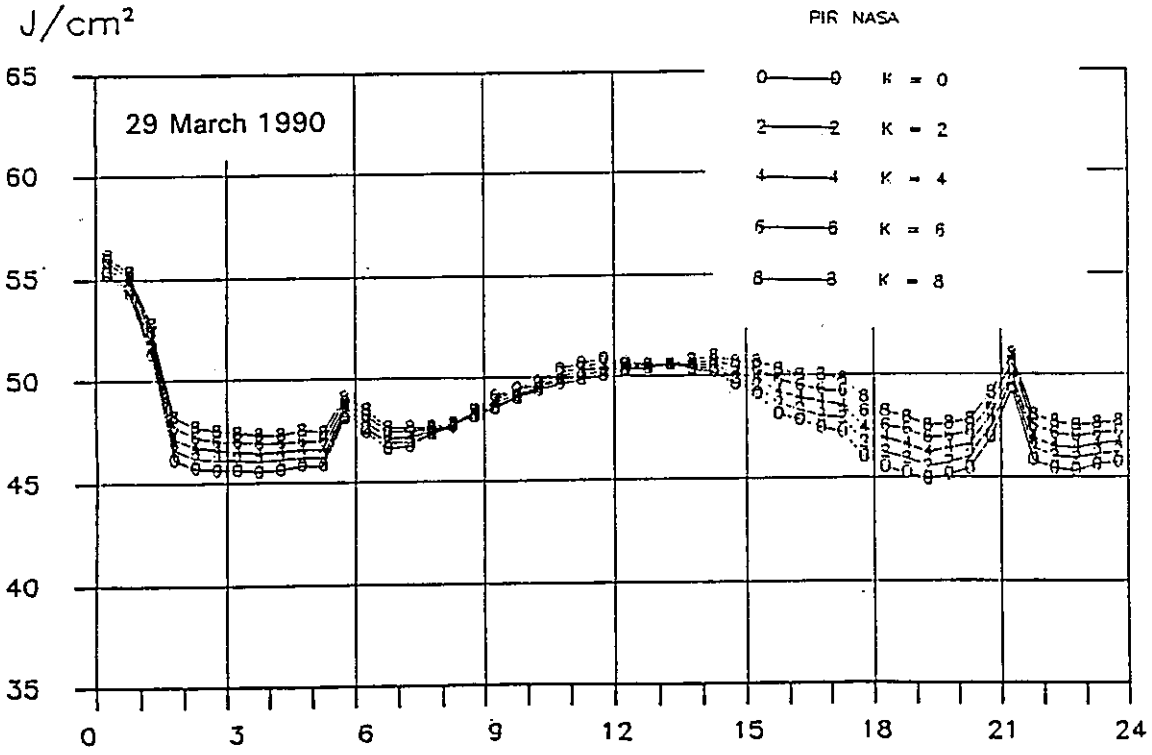

Fig. 36: Influence of the correction factor k on the diurnal cycle of A, 29 March 1990. NASA pyrgeometer

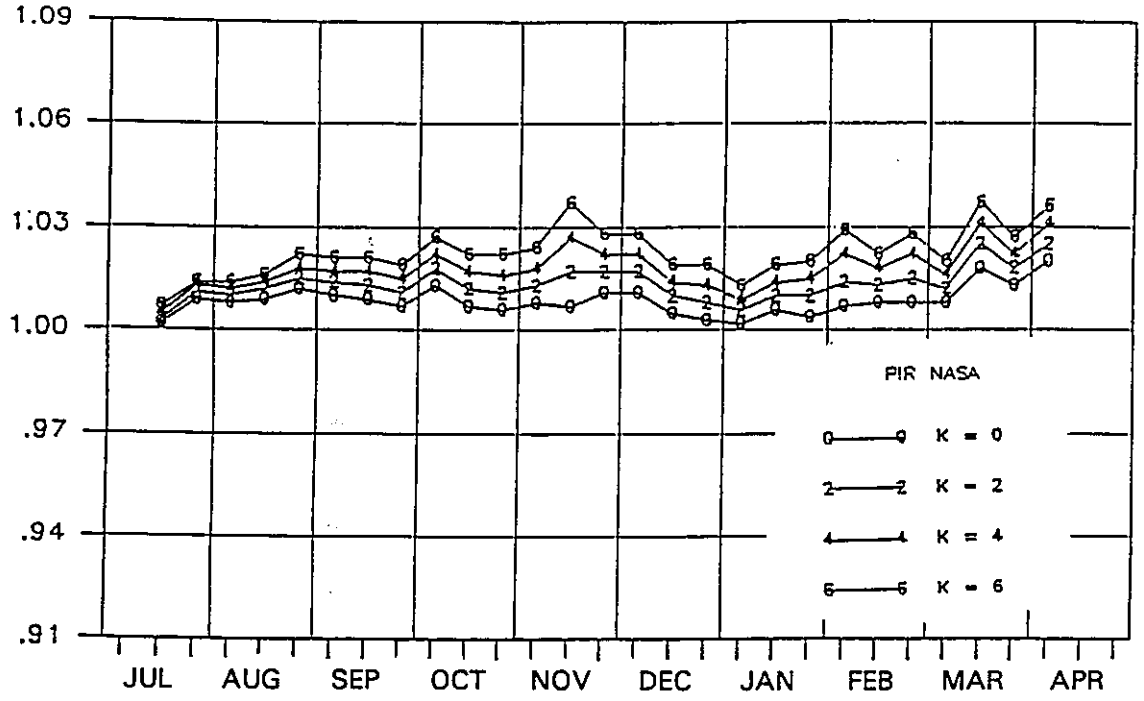

Fig. 37: Influence of the correction factor k on the diurnal cycle of A, 1989/90. NASA pyrgeometer

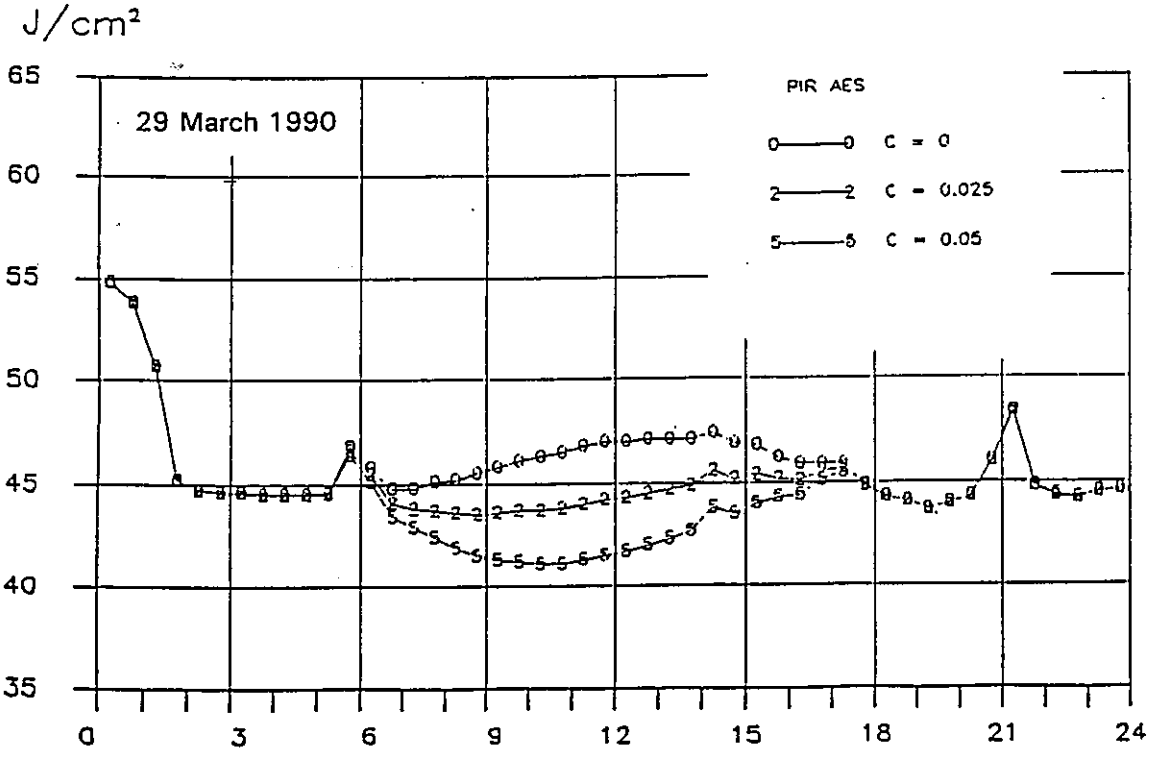

Fig. 38: Influence of the correction factor c on the diurnal cycle of A, 29 March 1990. AES pyrgeometer

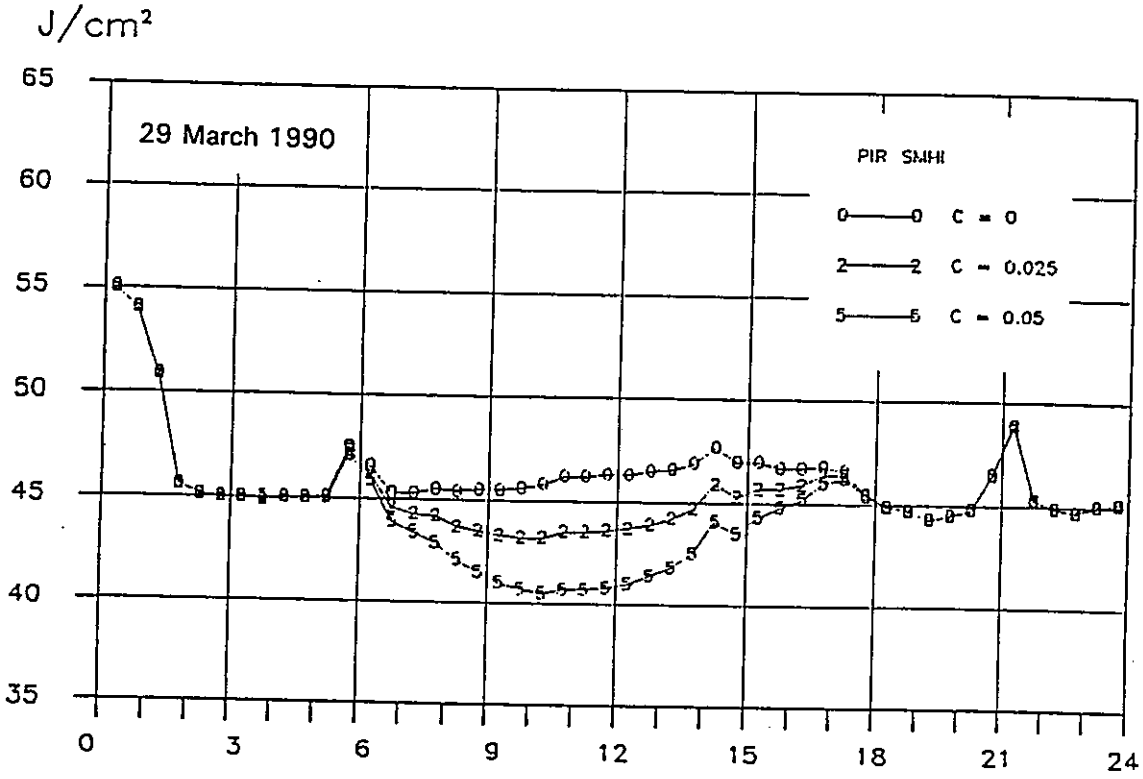

Fig. 39: Influence of the correction factor c on the diurnal cycle of A, 29 March 1990. SMHI pyrgeometer

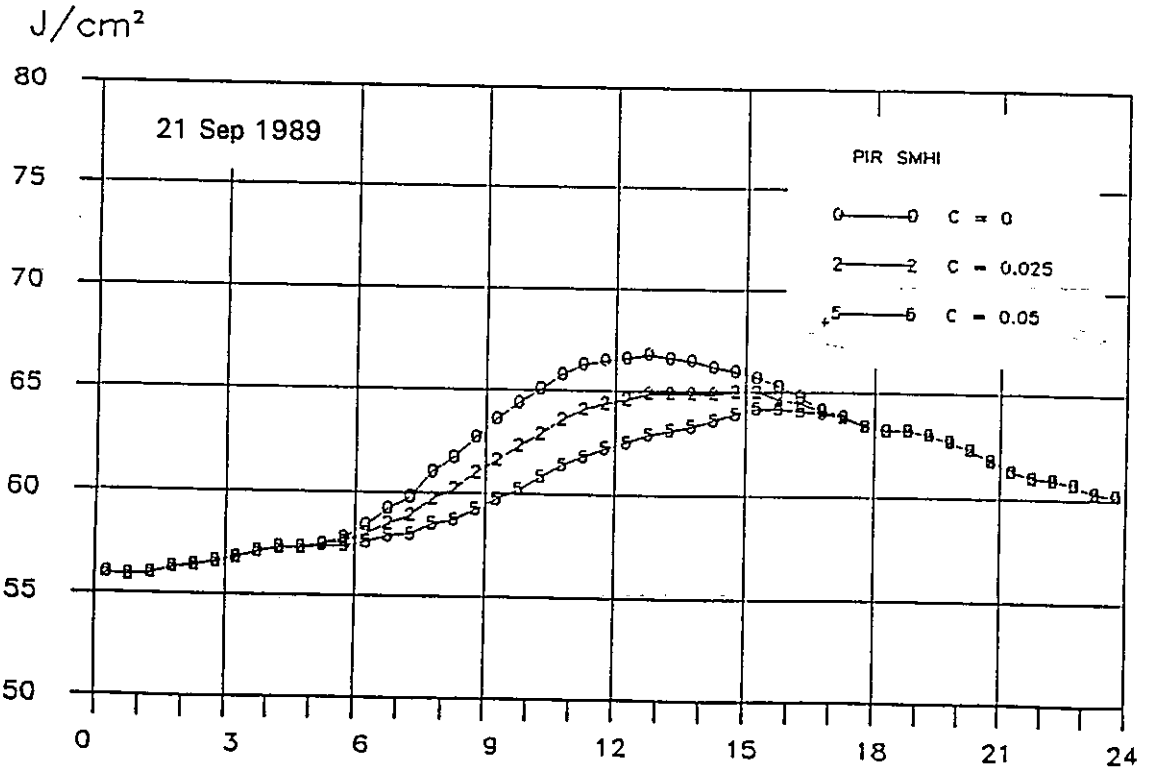

Fig. 40: Influence of the correction factor c on the diurnal cycle of A, 21 September 1989. Non-shaded SMHI pyrgeometer

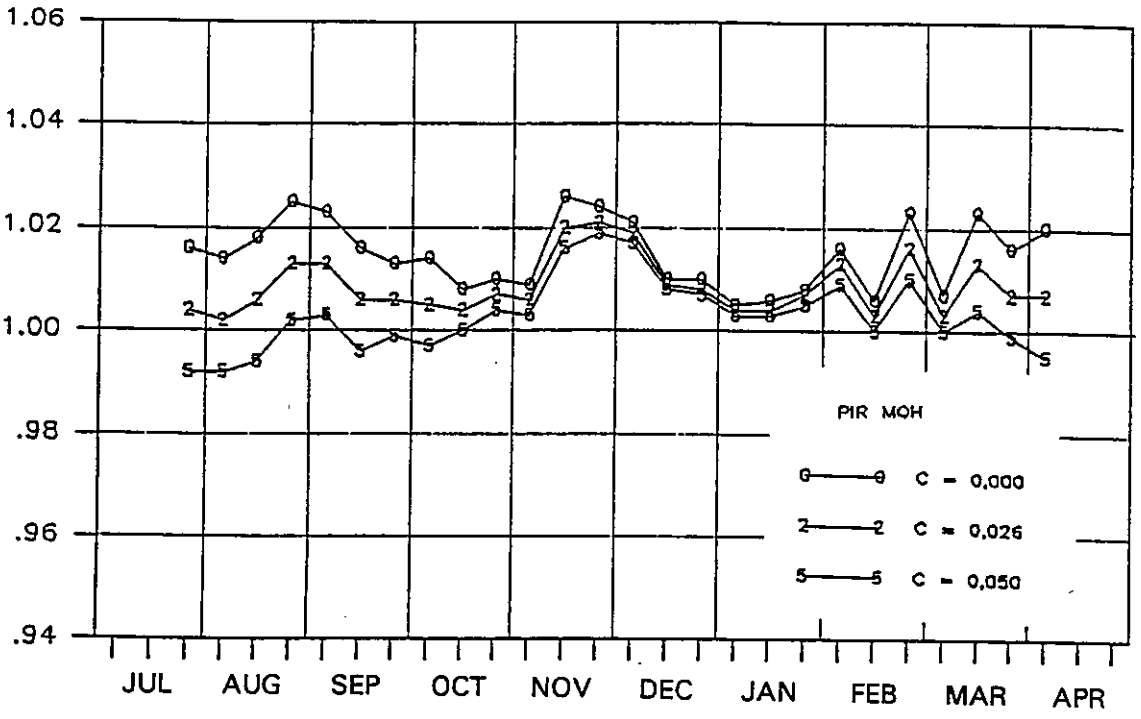

Fig. 41: Influence of the correction factor c on the seasonal variation of A, 1989/90. MOH pyrgeometer

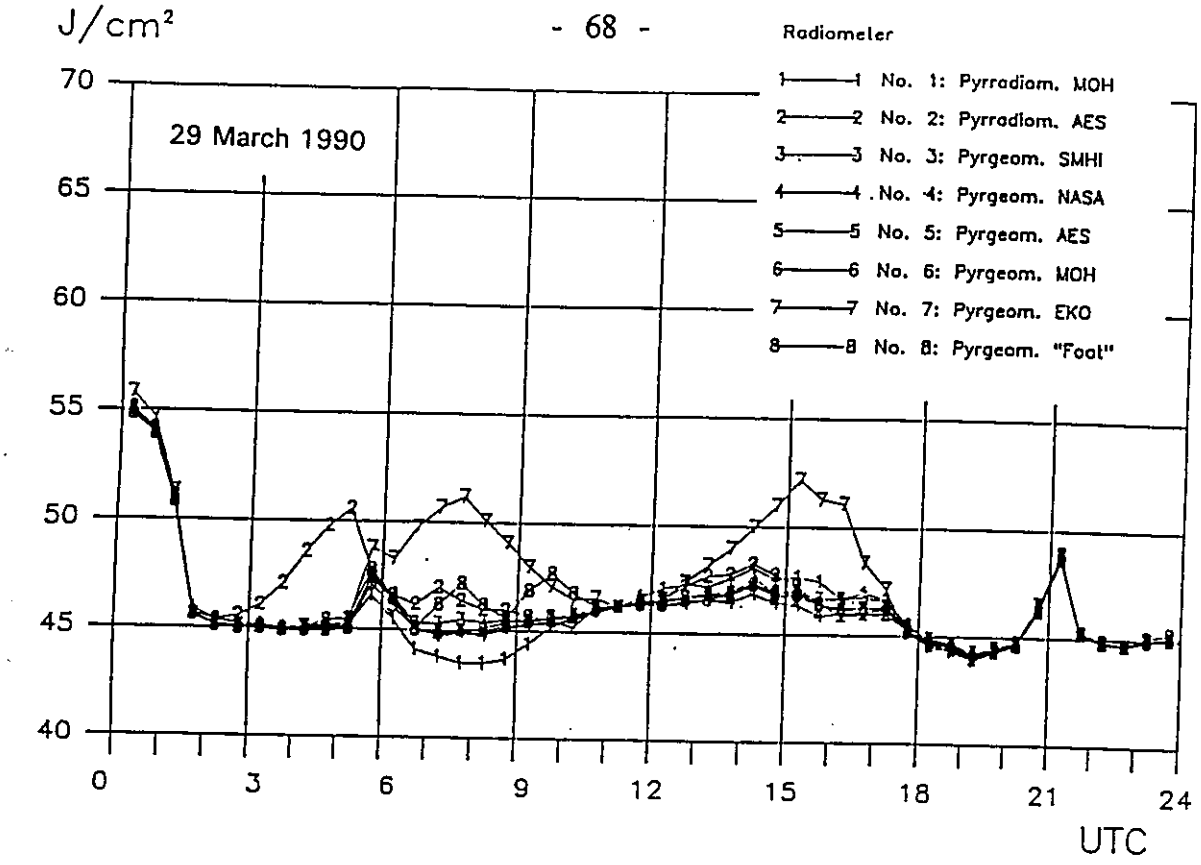

Fig. 42: Diurnal cycle of halfhourly sums of A on 29 March 1990, generated with the adjustment method

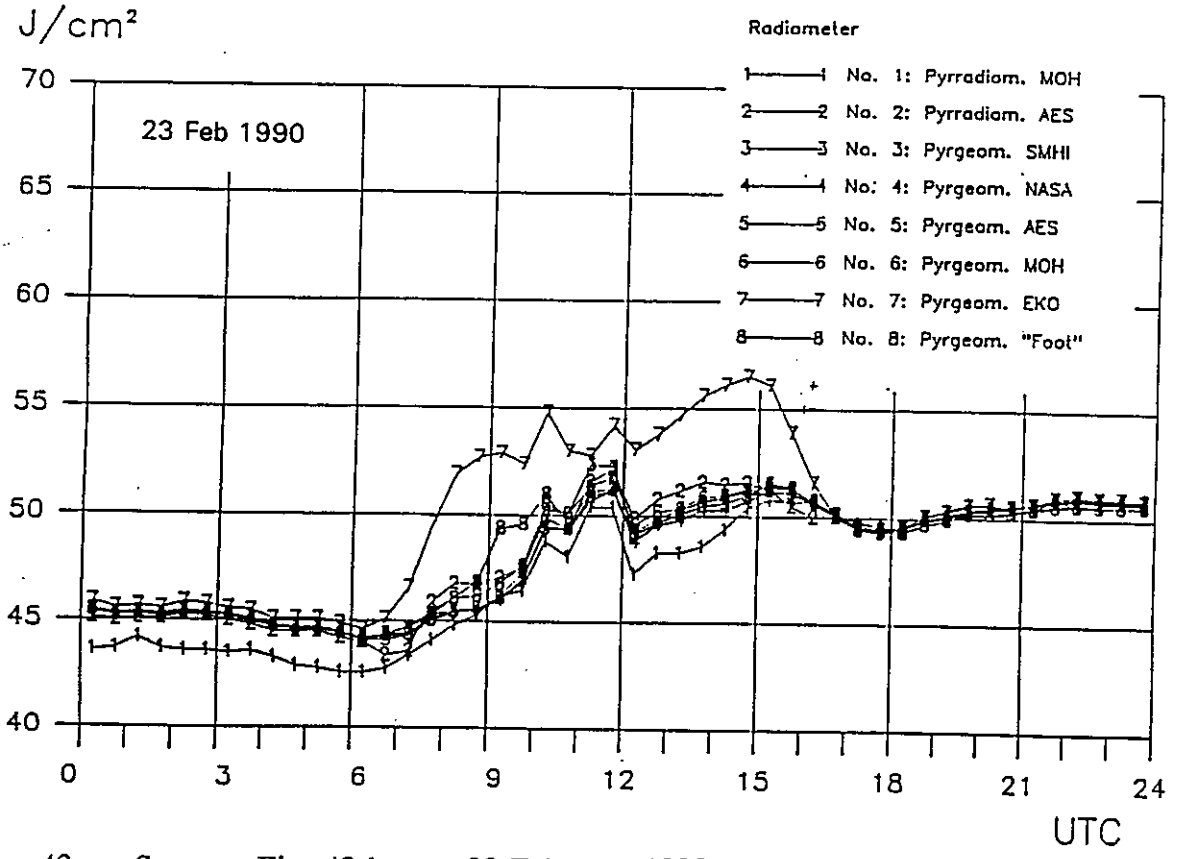

Fig. 43: Same as Fig. 42 but on 23 February 1990

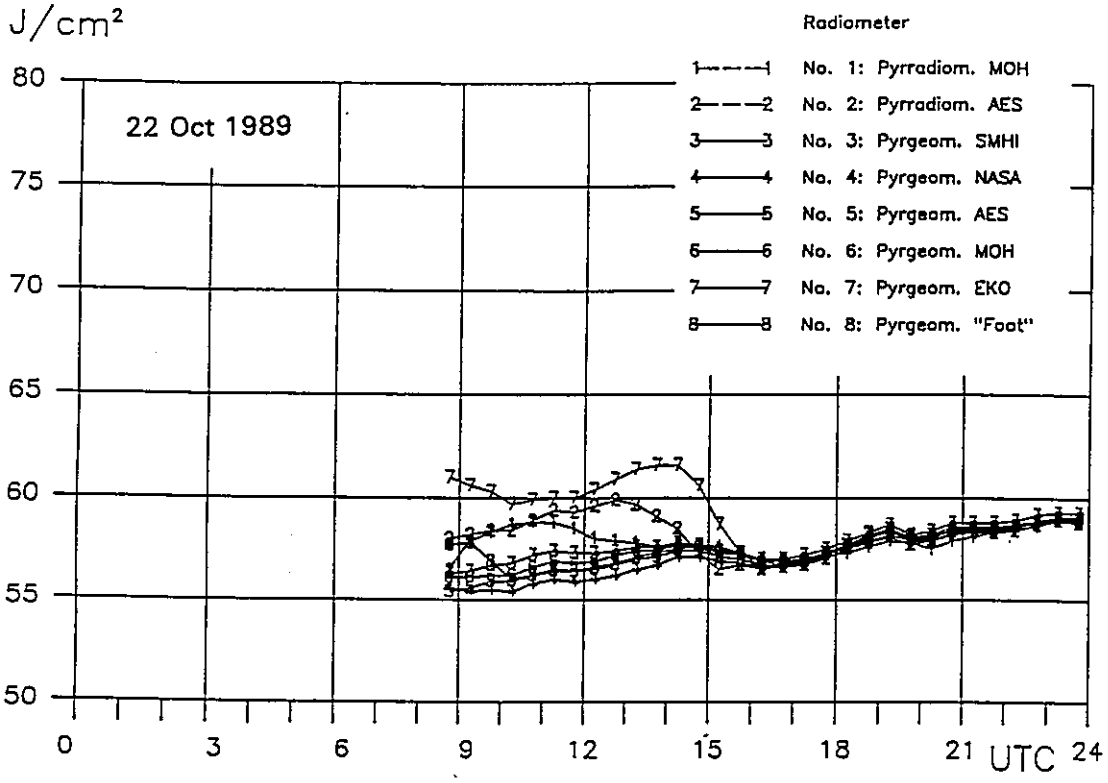

Fig. 44: Same as Fig. 42 but on 22 October 1989

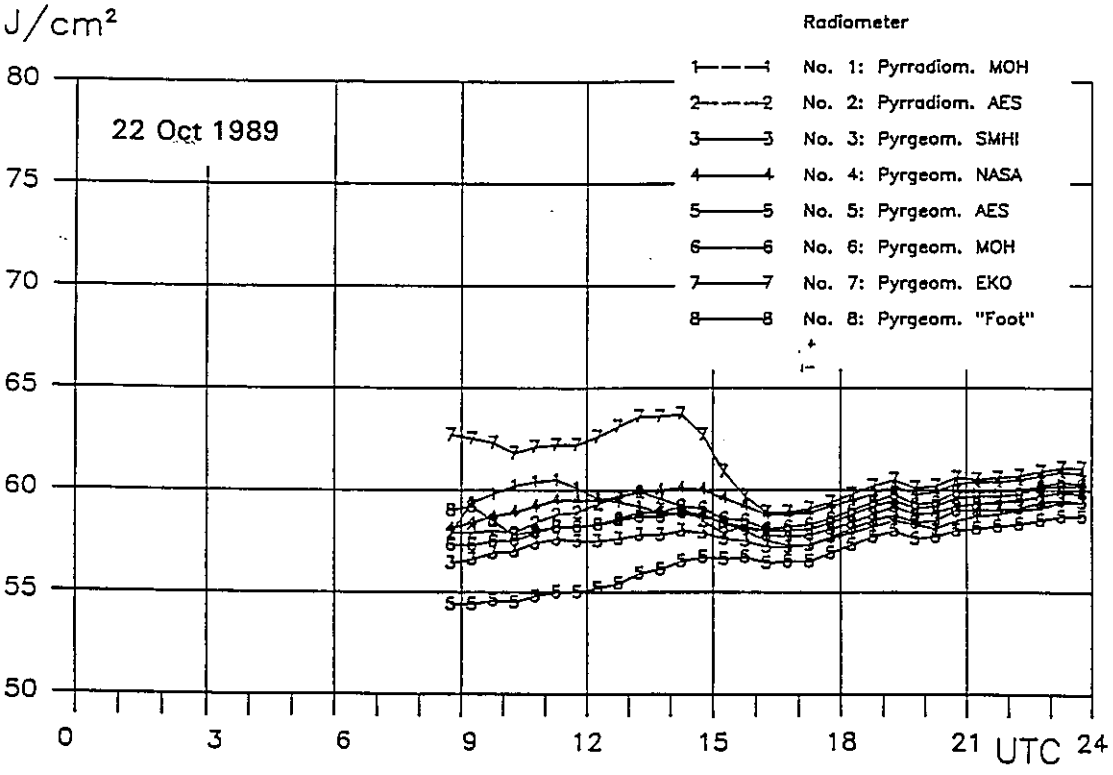

Fig. 45: Diurnal cycle of halfhourly sums of A on 22 October 1989 without adjustment

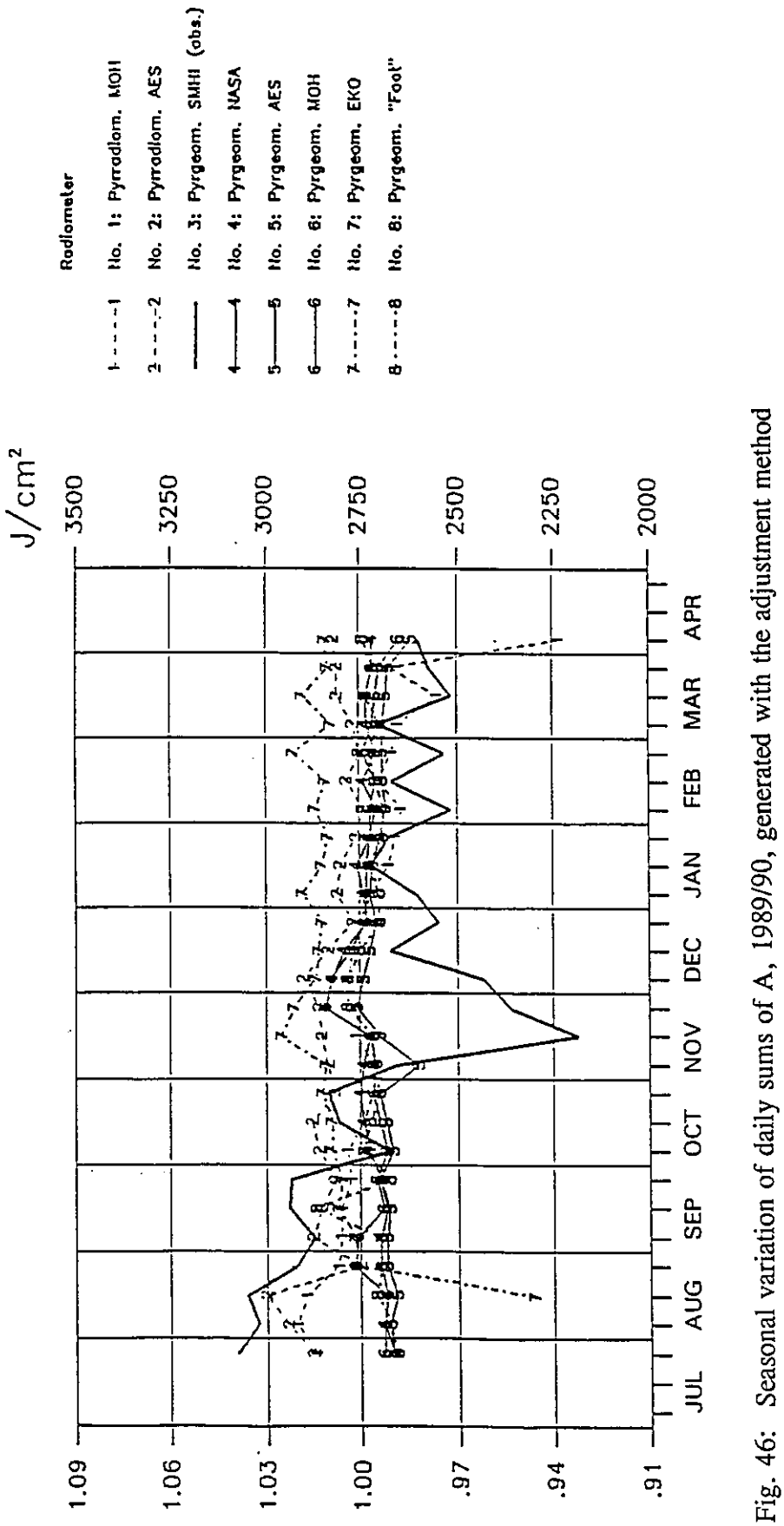

Fig. 46: Seasonal variation of daily sums of A, 1989/90, generated with the adjustment method

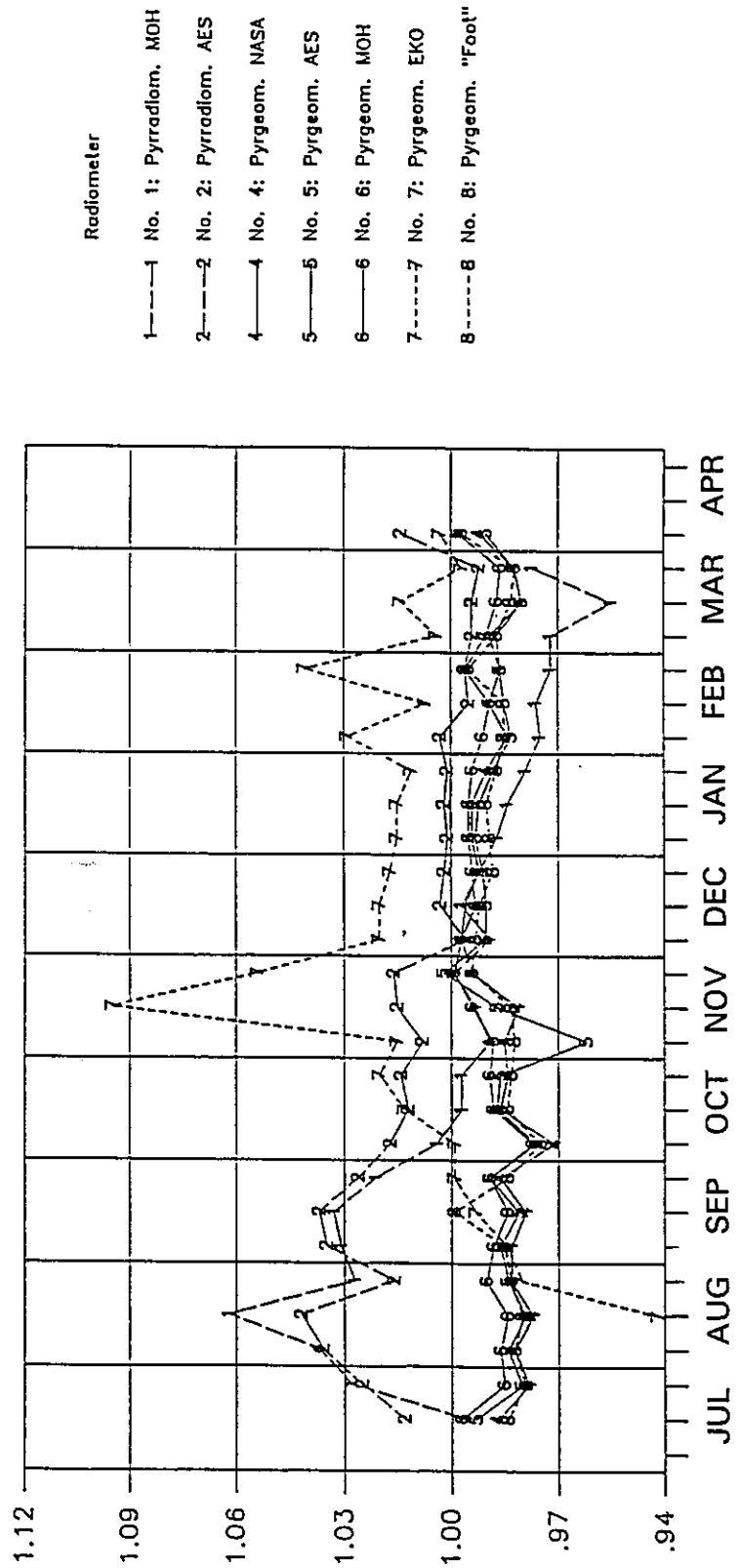

Fig. 47: Same as Fig. 46 but A-sums from 0930 to 1330 UTC

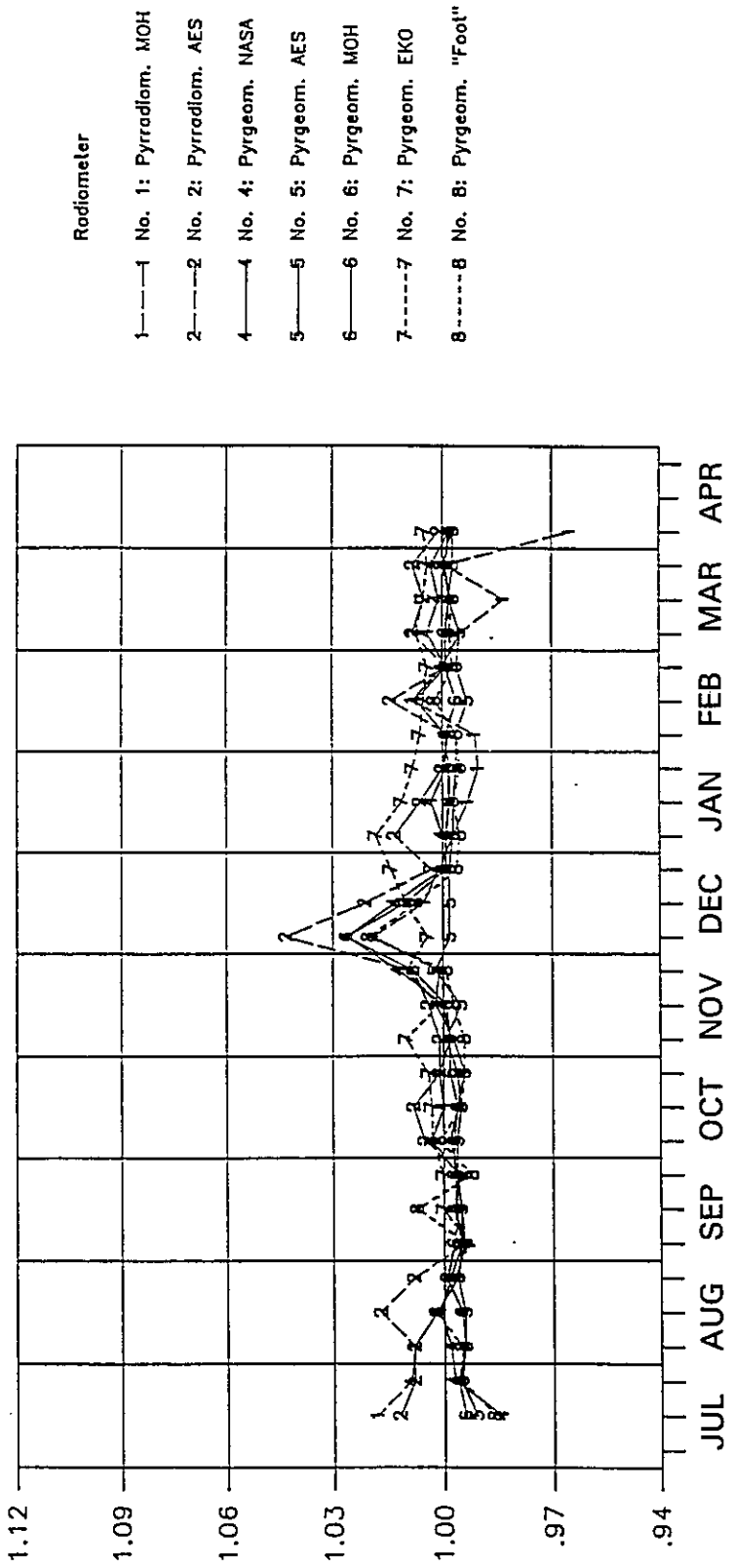

Fig. 48: Same as Fig. 46 but A-sums from 1800 to 2400 UTC